DISEASES AND DISORDERS

Differential pathological dynamics triggered by distinct Parkinson patient–derived α-synuclein extracts in nonhuman primates

R. Kinet[1]†, M. Bourdenx[1]†‡, S. Dovero[1], M. Darricau[1], M.-L. Arotcarena[1], S. Camus[1], G. Porras[1], M.-L. Thiolat[1], I. Trigo-Damas[2,3], S. Bohic[4], M. Morari[5], E. Doudnikoff[1], M. Goikoetxea[6], S. Claverol[7], C. Tokarski[7], N. Kruse[8], B. Mollenhauer[8,9], C. Estrada[10,11], N. Garcia-Carrillo[12], M. T. Herrero[10,11], M. Vila[3,13,14,15], J. A. Obeso[2,3,16], E. Bezard[1]*§, B. Dehay[1]*§

The presence of α-synuclein (α-syn) aggregates, such as Lewy bodies in patients with Parkinson's disease (PD), contributes to dopaminergic cell death. Injection of PD patient–derived α-syn in nonhuman primates has illustrated the exquisite vulnerability of primate dopaminergic neurons. Here, we aimed to elucidate the temporal and spatial pathological changes induced by two distinct α-syn pathogenic structures, having large or small sizes. To unravel the underlying molecular pathways, we conducted a proteomic analysis of the putamen and the entorhinal cortex, two brain regions carrying notable α-syn pathology. We demonstrate that distinct assemblies of α-syn aggregates drive unique pathogenic changes that ultimately result in a comparable extent of nigrostriatal degeneration at the level of nigral dopaminergic neuron cell bodies and striatal dopaminergic terminals. More broadly, our findings identify pathogenic trajectories associated with large or small α-syn aggregates, suggesting the existence of several possible concomitant pathogenic routes in PD.

INTRODUCTION

Characterizing animal models at different stages of disease progression is critical to understanding the course of neurodegenerative pathologies such as Parkinson's disease (PD). While accumulation of misfolded α-synuclein (α-syn) is central to PD, its presence does not always directly correlate with neuronal death. Other mechanisms beyond α-syn aggregation may, therefore, significantly contribute to neurodegeneration in PD (1). In addition to calling Braak's hypothesis into question (2), this finding urges the development of animal models that replicate that specific disease feature. Over the last decades, several nonhuman primate (NHP) models of PD have been characterized to better understand (3) and mimic as closely as possible (4) PD pathology progression and characteristics. These include the use of aged animals (5), toxins (6), viral vector–mediated gene delivery (7, 8), recombinant or patient-derived α-syn injections (9), or genetic modifications (10, 11),

PD patient–derived α-syn assemblies have been used as pathogenic triggers in vitro (12), in mice (13, 14) and NHPs (14–16), making it an inestimable tool for modeling PD. Previously, we showed that intrastriatal injection of patient-derived α-syn fractions containing either the large aggregates (LA fraction, also known as Lewy bodies) or the small aggregates (SA fraction, formed by soluble α-syn plus 10% aggregated α-syn with a different amyloid structure) led to the same extent of dopaminergic neurodegeneration in NHP but not in mice (14). The pathological profile observed in this 2-year post–striatal injection study suggested differential activation of cellular and metabolic pathways, underscoring the multifactorial nature and complexity of this synucleinopathy (14). However, a time-course study following LA and SA fraction injections is necessary to support this claim further.

This study aimed to investigate the molecular mechanisms triggered by the intrastriatal injections of patient-derived LA or SA fractions in the same NHP cohort at 6, 12, and 24 months postinjection, with in-depth analyses of more than 180 variables obtained from behavioral, histological, biochemical, transcriptional, and biophysical approaches applied to several brain areas for each individual. The results highlight distinct dynamics of pathogenic alterations between the LA and SA groups, particularly affecting synaptic modulation in the putamen and mitochondrial homeostasis in the entorhinal cortex.

[1]Univ. Bordeaux, CNRS, IMN, UMR 5293, F-33000 Bordeaux, France. [2]HM CINAC, HM Puerta del Sur, Fundación HM Hospitales and CIBERNED and CEU-San Pablo University, Madrid, Spain. [3]Center for Networked Biomedical Research on Neurodegenerative Diseases (CIBERNED), Instituto Carlos III, Madrid, Spain. [4]Univ. Grenoble Alpes, Synchrotron Radiation for Biomedicine (STROBE), Grenoble, France. [5]Department of Pharmaceutical and Pharmacological Sciences, University of Padova, Padova, Italy. [6]CIC NanoGUNE BRTA, Tolosa Hiribidea 76, 20018 Donostia-San Sebastián, Spain. [7]Univ. Bordeaux, Bordeaux Proteome, Bordeaux, France. [8]University Medical Center Goettingen, Institute of Neuropathology, Goettingen, Germany. [9]Paracelsus-Elena-Klinik, Kassel, Germany. [10]Clinical and Experimental Neuroscience Unit, School of Medicine, Biomedical Research Institute of Murcia (IMIB), University of Murcia, Campus Mare Nostrum, 30100 Murcia, Spain. [11]Institute of Research on Aging (IUIE), School of Medicine, University of Murcia, 30100 Murcia, Spain. [12]Centro Experimental en Investigaciones Biomédica (CEIB), Universidad de Murcia, Murcia, Spain. [13]Neurodegenerative Diseases Research Group, Vall d'Hebron Research Institute (VHIR), Barcelona, Spain. [14]Department of Biochemistry and Molecular Biology, Autonomous University of Barcelona (UAB), Barcelona, Spain. [15]Catalan Institution for Research and Advanced Studies (ICREA), Barcelona, Spain. [16]CEU, San Pablo University Madrid, E-28938 Mostoles, Spain.
*Corresponding author. Email: erwan.bezard@u-bordeaux.fr (E.B.); benjamin.dehay@u-bordeaux.fr (B.D.)
†These authors contributed equally to this work.
‡Present address: UK Dementia Research Institute, University College London, London WC1E 6BT, UK.
§These authors contributed equally to this work.

RESULTS

Striatal dopamine denervation kicks in earlier in LA-exposed NHPs

To determine the pathological dynamics induced by distinct patient-derived α-syn extracts in a species closer to humans, 37 adult baboons

(*Papio papio*) were allocated to a control group (*n* = 7), an LA group (*n* = 18), and an SA group (*n* = 12), receiving 100 µl of bilateral injection of PD patient–derived LA or SA fractions, respectively, in the putamen.

In our prior work (*14*), we extensively characterized those α-syn extracts from patients with PD, naming them LB and noLB (*14*). However, such nomenclature required amendment because we incorrectly assumed the absence of aggregated α-syn in SA fractions. The current terminology, instead, accounts for the amyloid fibril structure (*14*). We reported that LA fractions (formerly LB) primarily contain ~90% of large aggregated α-syn fibrils, whereas SA fractions (formerly noLB) are made of soluble α-syn (90%) and ~10% of small amyloid structures not found in LA fractions (*14*). Moreover, ultrastructural examination of SA and LA fractions by atomic force microscopy (AFM) (fig. S1A) and by electron microscopy (fig. S1B) confirmed structural differences, which specifically revealed the presence of larger aggregates in LA samples compared to those in SA samples. We confirmed that sonication for 5 min before injection disrupted LA into fibrillar fragments with an average size of 62.52 nm (fig. S1C). The α-syn content quantified by enzyme-linked immunosorbent assay (ELISA) was 41.33 pg/µl for SA and 24.52 pg/µl for LA. To allow comparison between experimental groups, we diluted both pools of fractions to the least concentrated pool (24 pg/µl) before in vivo injections.

To follow the pathology kinetics, experimental groups were terminated at 6, 12, and 24 months after surgery (control, *n* = 7; LA, *n* = 6 for each time point; and SA, *n* = 4 for each time point) (Fig. 1A). Nigrostriatal integrity was assessed by tyrosine hydroxylase (TH) staining, revealing a significant decrease in TH surface level in the substantia nigra (SN) of LA.24mo and SA.24mo groups compared to controls (Fig. 1, B and C), as previously reported (*14*). Stereological counts of TH-positive cells in the SN confirmed the lack of difference in dopamine cell loss between the LA and SA groups (−15.1 and −15.7%, respectively) (Fig. 1, D and E). The covariation of both endpoints in the LA and SA groups suggests that SN dopaminergic lesions are primarily localized within the dendritic arborization. Two years after administration, LA- and SA-injected baboons displayed significant striatal dopaminergic terminal loss in the putamen (Fig. 1, F and G) and the caudate nucleus (Fig. 1, F and H).

At 12 months, both LA- and SA-injected groups showed similar reduction in dopaminergic terminals (~17%), albeit only the LA group reached statistical significance. This phenotype, indicative of ongoing neurodegenerative processes, resembles a premotor stage of PD, characterized by less than the 45% loss of TH striatal innervation, at least below the threshold required for the onset of parkinsonism (*17*). The kinetics between the LA and SA groups (fig. S2, A to D) appear to be very similar, although it remains to be determined now whether distinct pathological mechanisms may be involved.

Cortical α-syn pathology begins earlier in LA-exposed NHPs

We investigated the levels of total α-syn (Fig. 2A) and α-syn phosphorylated at serine-129 (pSyn) (Fig. 2B), taken as a surrogate marker of α-syn pathology within 17 brain regions (Fig. 2C). Total α-syn (Fig. 2, A and C) globally decreased over time, except in the hippocampus. In the caudate nucleus, echoing the TH denervation data, α-syn progressively decreased from as early as 12 months in the LA group up to 24 months, ultimately reaching similar levels in both the LA and SA groups (−16.15% for LA.24mo and −15.65% for

SA.24mo compared to that in control). A time-dependent increase in total α-syn was found only in the hippocampus, which was more pronounced in the SA group compared to that in the LA group (Fig. 2D). pSyn immunoreactivity increased, particularly in the cortical areas of both the LA and SA groups. Such an increase, however, started as early as 6 months in the LA group (Fig. 2, B and C). The entorhinal cortex (Fig. 2, F and G, and fig. S3A), confirmed by biochemical techniques (fig. S2E), and parahippocampal cortex (Fig. 2, H and I, and fig. S3B) were significantly the most affected areas (*z*-score > 2). Transient elevations of pSyn were also observed in the hippocampus, although pSyn immunoreactivity peaked earlier in LA (6 months) than in SA (12 months) groups (fig. S3C). Together, these results suggest that striatal injections of LAs and SAs induce distinct temporal changes in α-syn and pSyn levels, with earlier development of pathology in LA-injected compared to that in SA-injected animals.

Differential pathological kinetics suggest an earlier start in LA-exposed NHPs

We conducted a thorough investigation of the LA- and SA-exposed NHP brains. We analyzed multiple pathology-related variables, including endpoints related to nigrostriatal denervation, behavioral parameters, α-syn–related and non–α-syn–related pathology endpoints (in several brain areas), and biological fluid α-syn measurements. A wide array of techniques was used, including ethology, immunohistochemistry, histology, biochemistry, synchrotron radiation x-ray fluorescence (SR-XRF) spectrometry (Fig. 3A), which allowed for the collection of 180 variables for each individual, as previously described (*14*) (see Fig. 3B for variable abbreviation nomenclature and table S1 for individual data). We extracted the variables that significantly differed between the control and the LA or SA groups from this dataset. We plotted them over time (Fig. 3C), irrespective of the direction of the change. Six months after injection, the LA and SA groups differed from the control group for 5 and 11 variables, respectively, a difference that rose to 44 and 31 variables, respectively, at 24 months after injection. Overall, this pattern is suggestive of a progressive disease phenotype (Fig. 3C). Second, to shed light on the different pathways affected at each time point, we grouped the variables into nine relevant categories (Fig. 3, D to F, and table S1). Such data organization unraveled different patterns in LA- and SA-exposed NHPs. It is interesting to notice the progressive differentiation between experimental and control groups over time, with higher number of significantly different variable 24 months after surgery for the majority of the categories (Fig. 3D). Six months after injection, LA-injected baboons showed nigrostriatal neurodegeneration that was associated with a larger modification in soluble α-syn–related compared to that in insoluble α-syn–related variables (Fig. 3E). Conversely, the SA group did not show neurodegeneration at 6 months, but larger changes in insoluble compared to that in soluble α-syn–related variables; moreover, alterations in proteostasis-related variables emerged (Fig. 3F). Twelve months after injection, the LA group showed larger nigrostriatal neurodegeneration which was associated with a progressive increase in the number of soluble and insoluble α-syn–related and basal ganglia dysfunction [i.e., γ-aminobutyric acid (GABA) and glutamate levels in Globus Pallidus Internus (GPi)] variables (Fig. 3E). The number of soluble α-syn–related and pSyn-related variables increased. Similarly, although no overt parkinsonism was observed, behavioral abnormalities kicked in, notably social withdrawal [as reported in 24-month baboons;
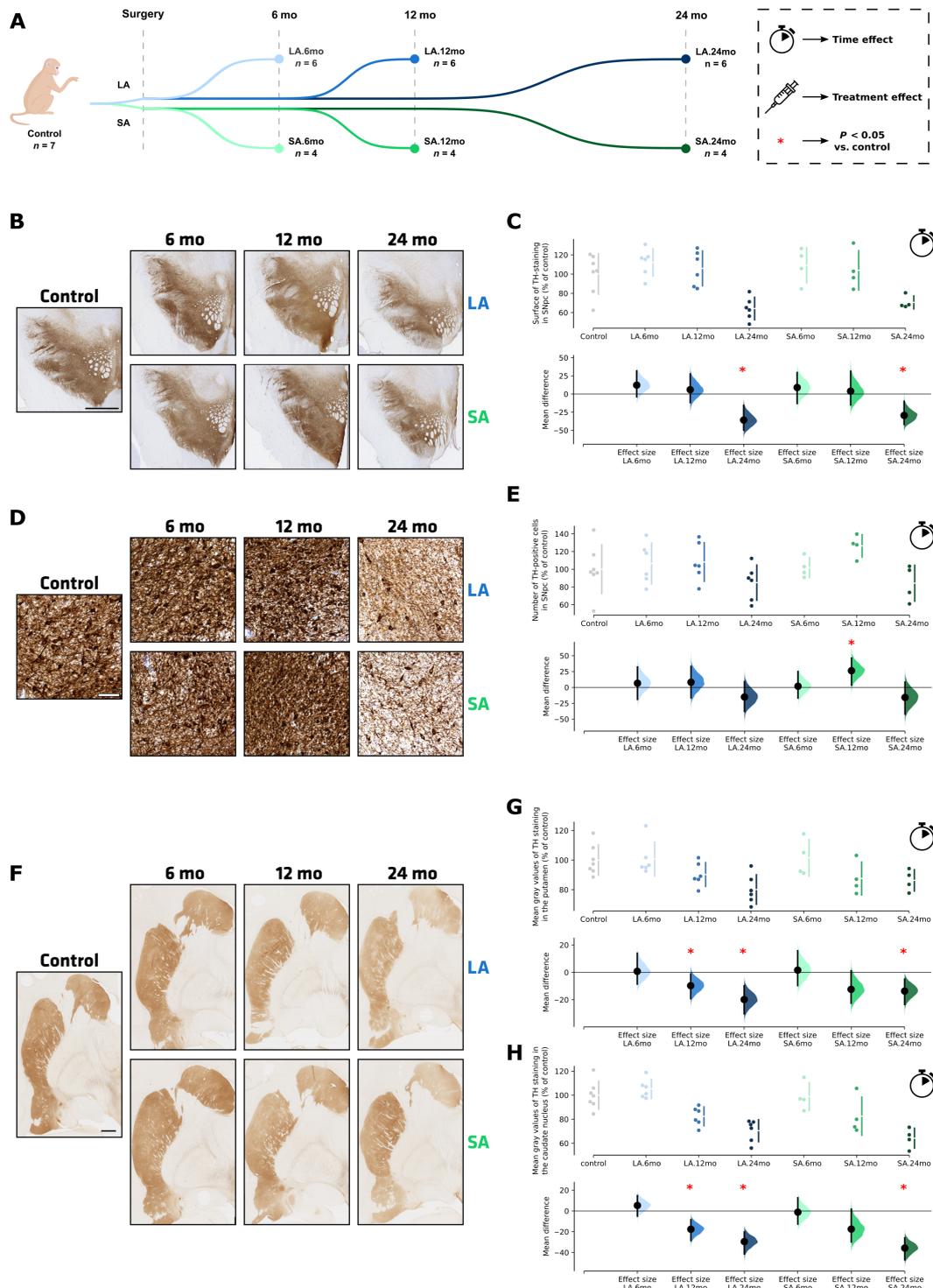
Fig. 1. Distinct nigrostriatal neurodegeneration pattern is observed after intrastriatal injection of patient-derived LA and SA fractions. (**A**) The study plan includes injection of brain-derived LA and SA fractions with termination time points at 6, 12, and 24 months after surgery. (**B**) Illustrative images and (**C**) scatter plots of nigral tyrosine hydroxylase (TH) surface immunostaining in the SN of control and LA/SA-injected NHPs are expressed as a percentage of controls. Scale bar, 500 μm. (**D**) Representative images and (**E**) quantification of TH-positive neurons by stereological counting in the SN of control and at different time points following intrastriatal injection of LA and SA fractions from Parkinson's disease patients. Scale bar, 200 μm. (**F**) Illustrative images and (**G** and **H**) scatter plots of striatal TH immunostaining in control and LA/SA-injected non-human-primates are expressed as a percentage of controls. Scale bars, 5 mm. Data are expressed as means ± SD, the bootstrapped mean difference with 95% confidence interval (CI; error bar) is shown on the bottom part of the graph. Statistical analysis was performed using a two-sided permutation t test. *P < 0.05 compared to control animals. mo, months.
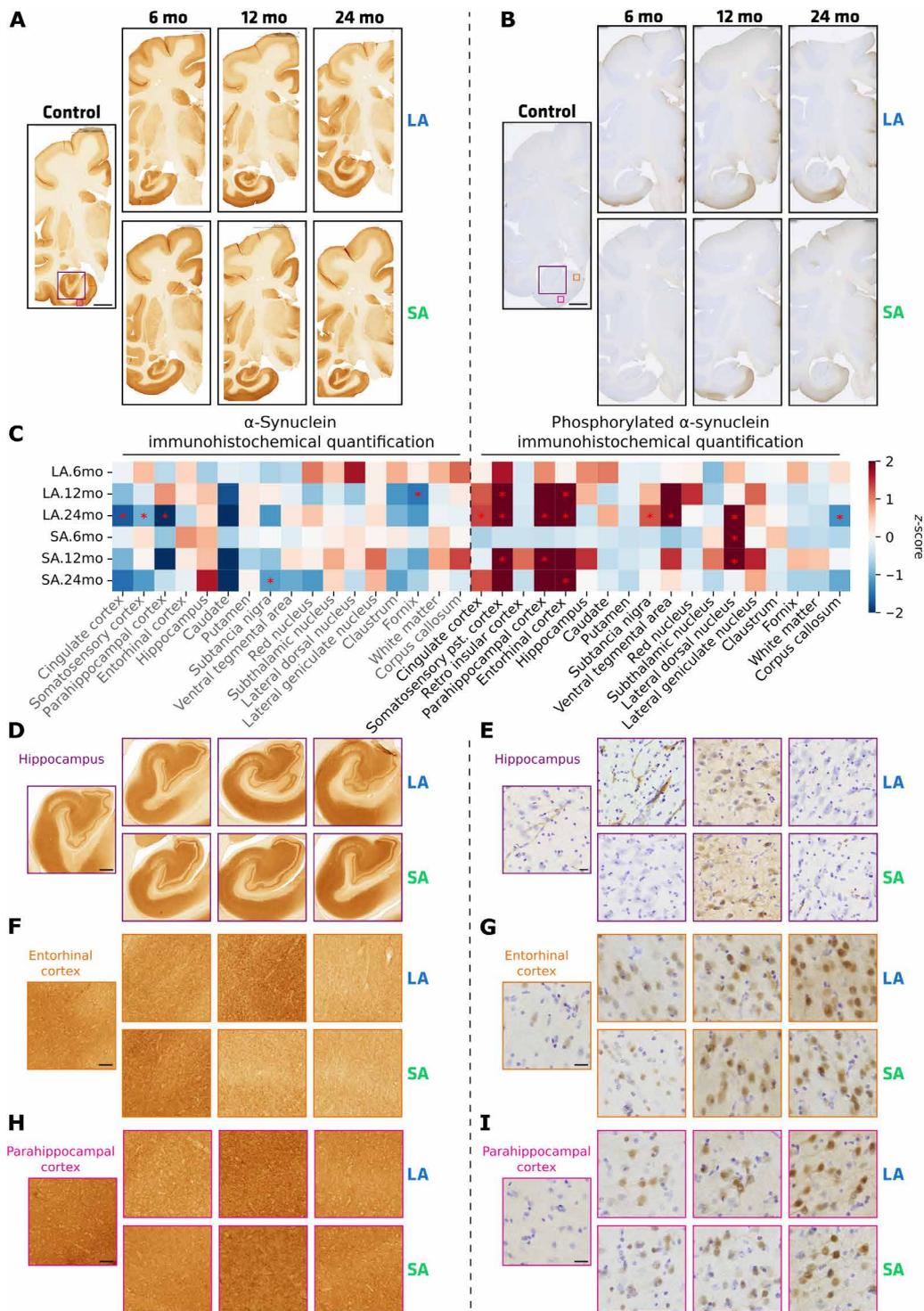
Fig. 2. Brain-wide analysis of α-syn pathology following intrastriatal injection of LA and SA fractions from patients with Parkinson's disease. (**A** and **B**) Illustrative image of (A) α-syn and (B) serine-129 phosphorylated α-syn (pSyn) staining. (**C**) Histological quantification in different brain regions of α-syn and pSyn represented as a z-score from the control mean and SD heatmap, and statistical analysis was performed using a two-sided permutation t test. *$P < 0.05$ compared to control animals. (**D** and **E**) Inset of illustrative images of (D) α-syn and (E) pSyn immunostaining in the hippocampus of control, SA-injected, and LA-injected animals. (**F** and **G**) Inset of illustrative images of (F) α-syn and (G) pSyn immunostaining in the entorhinal cortex of control, SA-injected, and LA-injected animals. (**H** and **I**) Inset of illustrative images of (H) α-syn and (I) pSyn immunostaining in the parahippocampal cortex of control, SA-injected, and LA-injected animals. Scale bars, (A and B) 8 mm, (D) 1 mm, (E, G, and I) 20 μm, and (F and H) 100 μm. mo, months.

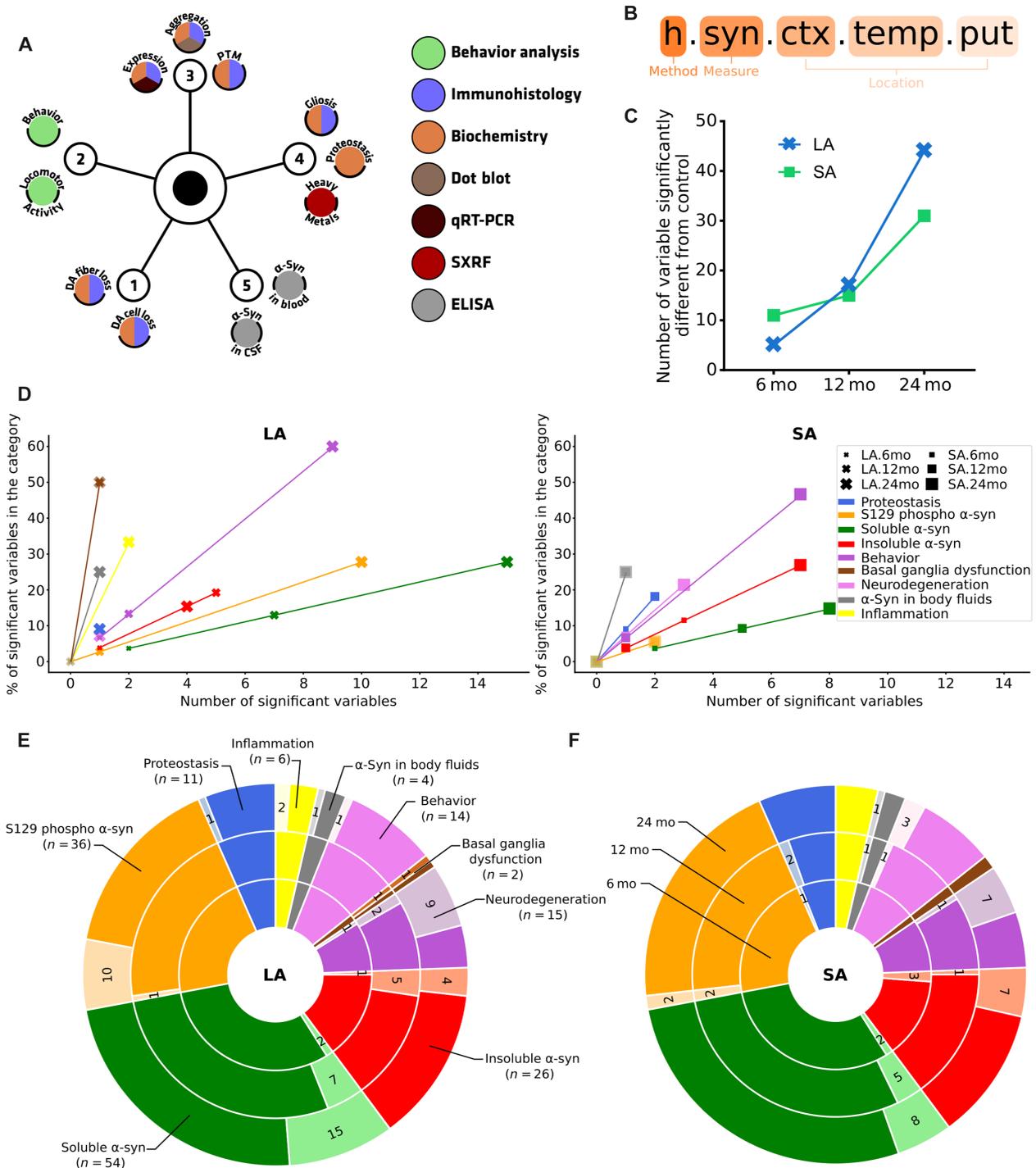**Fig. 3. Pathological-related variable differences between LA and SA groups.** (**A**) Graphical representation of the different types of variables analyzed in this study including (1) dopaminergic degeneration, (2) behavioral assessment, (3) α-syn–related pathology, (4) non–α-syn–related pathology, and (5) putative biomarkers. (**B**) Guideline for variable naming. (**C**) Analyses of the number of variables significantly different from the control group show an increase over time for both groups. (**D**) Scatter plots displaying the number of significant variables (*x* axis) and the percentage of significant variables of each category, including proteostasis, S129 phosphorylated α-syn, soluble α-syn, insoluble α-syn, behavioral, basal ganglia dysfunction, neurodegeneration, α-syn in body fluids, inflammation parameters (*y* axis), and the different time points (6, 12, and 24 months) with different size and symbols (cross for LA and square for SA) reveals a difference pattern in LA (left) and SA (right) groups. (**E** and **F**) Pie-doughnut charts showing the relative proportions of each variable investigated in the LA (E) and SA (F) groups. The total ring size refers to the relative proportions of variables investigated (*n* = 168) grouped by color category; the internal rings refer to the 6-month postinjection time point, the middle rings to the 12-month postinjection time point, and the external rings refer to the 24-month postinjection time-point groups. Significantly different variables in the LA and SA groups compared to those in controls at the three different time points postinjection (i.e., 6, 12, and 24 months) are represented in lighter color than nonsignificant ones. mo, months.

(*14*)]. LA-exposed NHPs collected at 24 months further worsened, with even more variables being significantly affected compared to controls (Fig. 3E). SA-exposed NHPs also showed a rise in the number of significantly affected variables at 24 months, but only those related to soluble α-syn and degeneration (Fig. 3F). While both groups displayed a comparable extent of nigrostriatal degeneration at 24 months, these data suggest an earlier start of the pathological process in LA-exposed NHPs, with SA-exposed animals displaying a less mature pathological profile than LA-exposed ones.

Proteomic analysis of putamen and entorhinal cortex reveals mechanistic differences

After highlighting the different pathway time courses, we further studied the spatial response (local and distant) to LA and SA injections and its modulation over time through unbiased mass spectrometry (MS)–based proteomics. Proteomic analysis was performed on two regions: (i) the putamen, which is the injection site and shows neurodegeneration (Fig. 1, F to H), and (ii) the entorhinal cortex, which is the region showing the most pronounced pSyn changes (Fig. 2G).

Pairwise comparisons in the putamen revealed that numerous proteins were differentially regulated under the various experimental conditions (Fig. 4A). Unlike the SA group, the number of up-regulated proteins diminished over time (i.e., from 6 to 24 months) in the LA group compared to that in the control group (Fig. 4A). The number of down-regulated proteins peaked 24 months after injection in both experimental groups. LA and SA groups shared the most differentially abundant proteins (DAPs) (*18*) at 24 months after injection, indicating a similar proteome profile at late stage (Fig. 4B). This similarity was confirmed by hierarchical clustering (Fig. 4C) because arranging the injection groups by time points revealed that, in the putamen, the core response is conserved irrespective of the type of α-syn injected. Protein-based clustering highlighted a major difference between early (6 and 12 months) and late (24 months) time points, reinforcing the results obtained on conserved DAPs (Fig. 4B).

Next, we used unsupervised dimensionality reduction [principal components analysis (PCA)] to capture proteome-wide variations across groups. PCA identifies principal components (PCs), or dimensions, that represent coordinated variations in protein abundance and are ordered by the amount of variance they explain. We then correlated these "proteomes axes" with previous experimental data. The Pearson correlation coefficient test revealed a strong correlation between PC3 values and many experimental neuropathology-related variables (Fig. 4D). PC3 also discriminated between experimental groups affected by PD patient–derived fractions and the other groups at 24 months (Fig. 4E), showing a divergent pattern at the 12-month time point (LA.12mo, 11.00%; and SA12.mo, −0.62%) (Fig. 4F). We selected the top 10% of proteins contributing to PC3, over the 95th percentile ($n = 138$) and under the 5th percentile ($n = 138$) (Fig. 4F). Gene ontology combined with network analysis showed that proteins involved in purine metabolism and synaptic organization were the most differentially expressed in the putamen, consistent with neurodegeneration events around the injection site (i.e., putamen) (Fig. 4, F and G) (*19*, *20*).

The same analysis was performed on the entorhinal cortex proteomic dataset. The number of up-regulated proteins increased progressively in the LA group, from 20 to 40 proteins up-regulated at 6 and 24 months, respectively (Fig. 5A). A group of 22 DAPs, composed of 14 up-regulated and 8 down-regulated proteins, was conserved

among the LA and SA groups at 12 and 24 months after injection, showing a similar maturation of the pathology (Fig. 5B). Also, the LA.12mo group shared more DAPs with the SA.12mo and SA.24mo groups than with the LA.24mo group, suggesting a different pathology trajectory for this group (Fig. 5B). The abundance of DAPs in the entorhinal cortex proteins was standardized as z-scores and hierarchically clustered (Fig. 5C). Group clustering showed similarities between the LA and SA groups 6 months after injection, and separation by α-syn–type injected after 12 months (when pathological α-syn starts to accumulate in this region; Fig. 2C). This highlights the different cellular response engaged by the two types of α-syn aggregates. From a temporal standpoint, the LA group at 24 months was grouped with SA groups at 12 and 24 months, indicating a faster progression of α-syn pathology in the entorhinal cortex of the SA group and consolidating the data from conserved DAPs analysis (Fig. 5B).

To study the dataset by multidimensional analysis, we performed PCA and correlated the results with experimental variables. PC2 correlated the most with the 180 pathological-related variables through the Pearson correlation (Fig. 5D). Furthermore, we could discriminate the patient-derived injection groups across time points (Fig. 5E). The explained variance of the PC2 revealed dynamic differences among experimental groups (Fig. 5F). The LA group progressively increased from −23.27% at 6 months to 8.40% at 12 months and to 11.68% at 24 months. The mean explained variance of the SA group rose from −14.88% at 6 months to 19.57% at 12 months, settling to 15.96% at 24 months (Fig. 5F). To further disentangle in network analysis, we selected the 10% of proteins having more impact on the PC3 explained variance, i.e., over the 95th percentile ($n = 134$) and under the 5th percentile ($n = 134$) (Fig. 5F). Unlike the putamen, the selection of multiple proteins from the entorhinal cortex PC2 is 10% related to the mitochondria and exocytosis process (Fig. 5G). This pattern is consistent with the central role of the mitochondria in caspase activation and cell death and distant spreading phenomenon involving α-syn exocytosis (Fig. 5, F and G) (*20*, *21*).

Alterations of synaptic markers in putamen occur early in SA

To validate our proteomic results, we explored the nature of dysregulated synaptic organization by measuring the expression of the postsynaptic density protein 95 (PSD-95) and the presynaptic density protein synaptophysin (*22*) in the putamen. PSD-95 expression levels (Fig. 6, A and B) showed a reduction in the LA groups compared to that in controls at 12 months (−50.1%) and 24 months (−24.0%) after injection. Conversely, in the SA groups, PSD-95 expression levels were reduced at 6 months (−54.3%), 12 months (−55.9%), and 24 months (−60.4%), indicating fast and strong postsynaptic alterations (Fig. 6B). Synaptophysin levels were unaffected in the LA groups (Fig. 6, A and C), whereas they gradually declined in the SA group at 12 months (−21.6%) and 24 months (−43.19%), suggesting a later decline in presynaptic elements following the rapid loss of postsynaptic compartments (Fig. 6B). Of interest, in the SA group at the latest time point (i.e., SA.24mo), PSD-95 levels negatively correlated with aggregated α-syn measured by dot-blot in the putamen [coefficient of determination (R^2) = −0.9817, $P = 0.0183$] (Fig. 6D), indicating that the increase in aggregated forms of α-syn is associated with a decrease in PSD95 expression. In addition, PSD95 expression positively correlated with three different α-syn soluble-related variables in the putamen (Fig. 6D). These findings suggest that changes in the expression levels of PSD95 may reflect
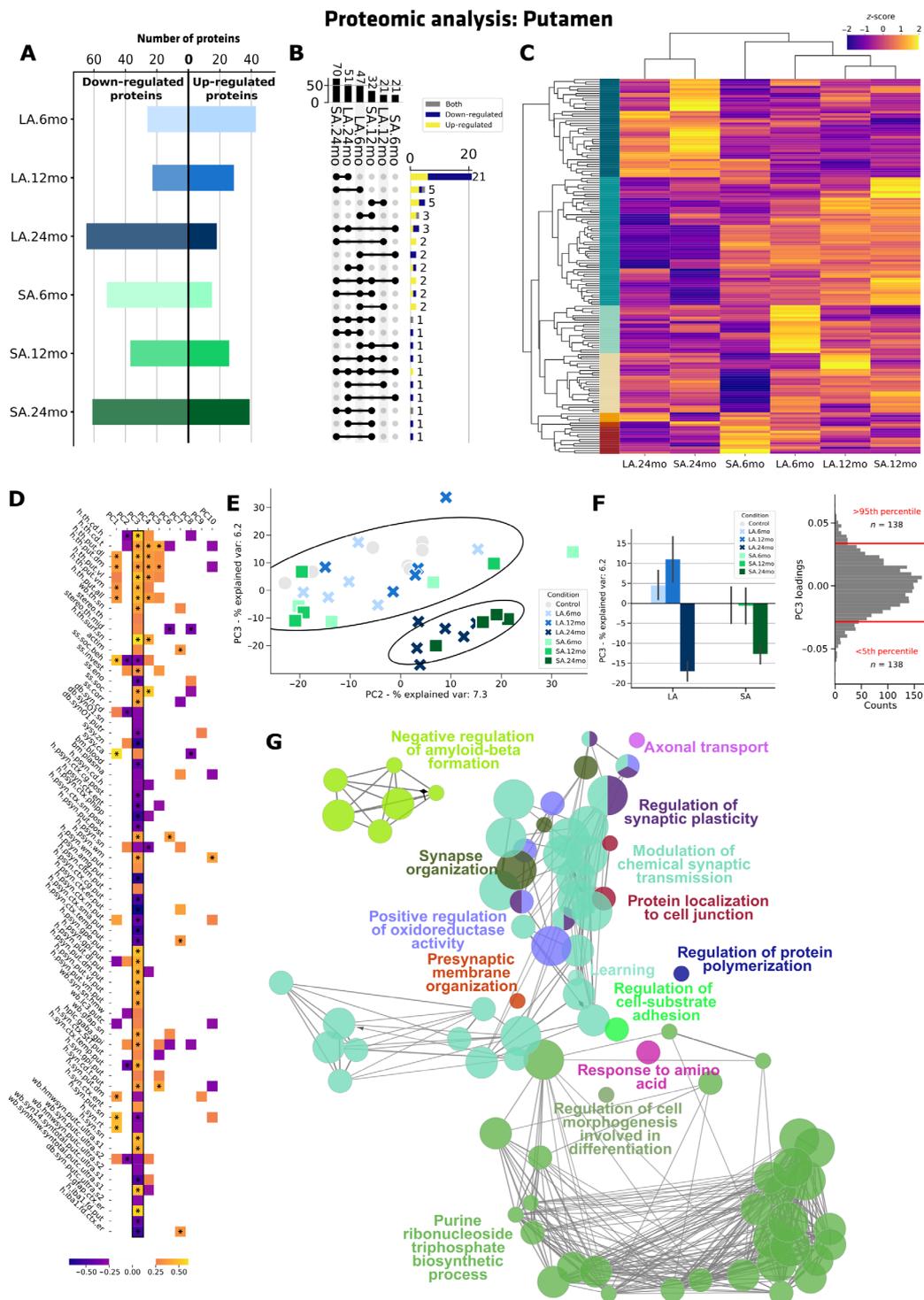
Fig. 4. Proteomic analysis of putamen protein samples shows differences in protein expression dynamics between the LA and SA groups over time. (A) Number of proteins significantly up-regulated or down-regulated in LA- and SA-exposed groups compared to control group. (**B**) UpSet plot of the differentially abundant proteins (DAPs) ($n > 1$) conserved in at least two groups, representing up-regulated (yellow) and down-regulated (blue) proteins in different groups. Each column corresponds to an experimental group set, and bar charts on top show the size of the set. Each row corresponds to a possible intersection: The filled-in cells show which set is part of an intersection. Also notice the lines connecting the filled-in cells: They show in which direction you should read the plot. (**C**) Heatmap and hierarchical clustering analysis based on changes in protein abundance compared to control. (**D**) Principal components analysis (PCA) of the proteomic dataset correlated with variables obtained from behavioral, histological, biochemical, transcriptional, and biophysical approaches. Pearson correlation between the individual scores in each principal component (PC) with the individual values of variable analysis, *$P < 0.05$. (**E**) Individual NHP values upon PC2 and PC3 drawing two clusters segregating animals injected 24 months before the others. (**F** and **G**) Network analysis of proteins under the 5th and above the 95th percentile of the PC3 ($n = 300$).
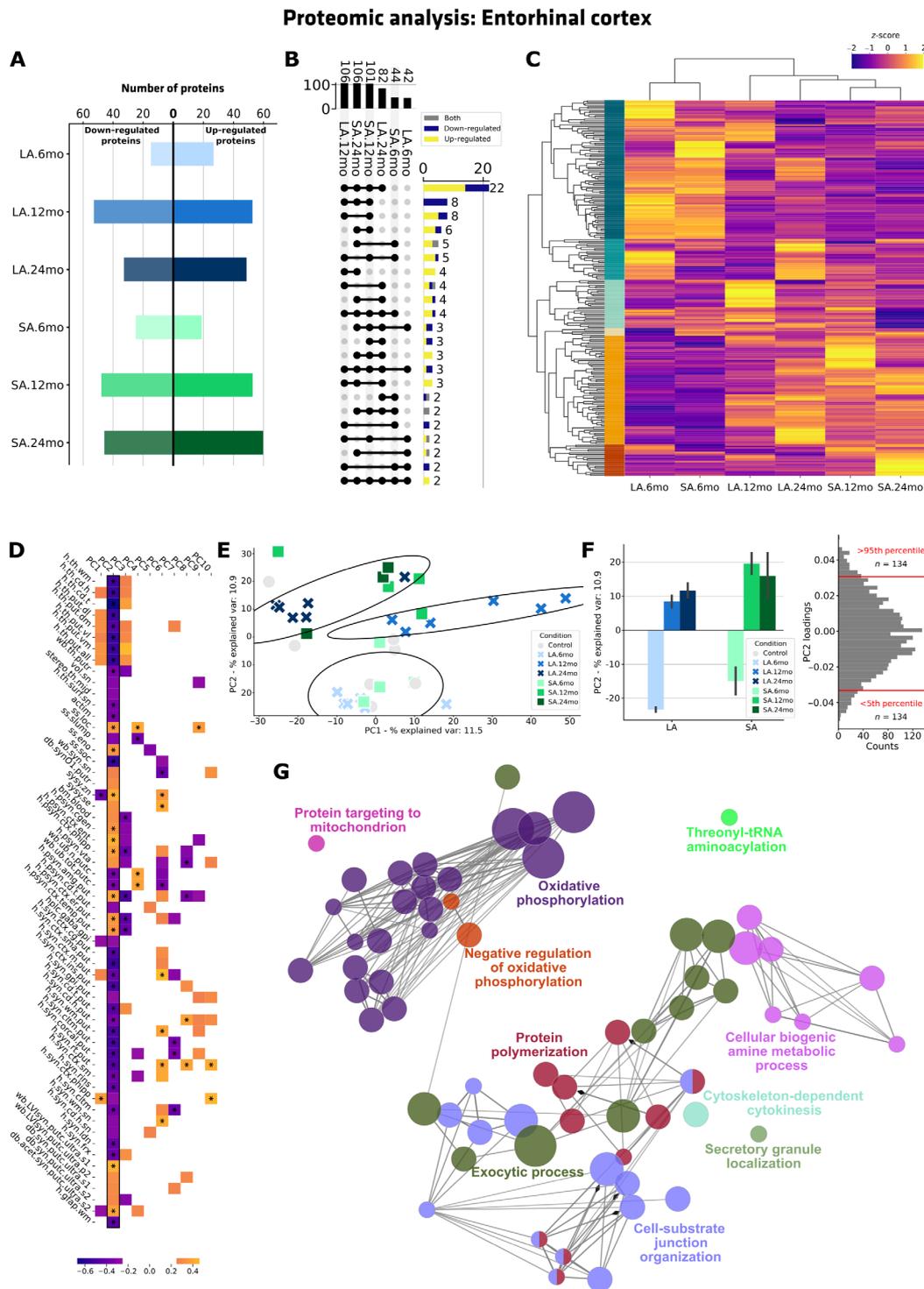
Fig. 5. Proteomic analysis of entorhinal cortex protein samples shows differences in protein expression dynamics between the LA and SA groups over time. (**A**) Number of proteins significantly up-regulated or down-regulated in LA- and SA-exposed groups compared to controls over time show similar ending numbers with differences in first-time points. (**B**) UpSet plot of the DAPs ($n > 1$) conserved in at least two groups, representing up-regulated (yellow) and down-regulated (blue) proteins up- and down-regulated in different groups. (**C**) Heatmap of all protein expression significantly up-regulated or down-regulated compared to control in the entorhinal cortex. (**D**) PCA of the proteomic dataset correlated with variables obtained from behavioral, histological, biochemical, transcriptional, and biophysical approaches. Pearson correlation between the individual scores in each PC with the individual values of variable analysis, *$P < 0.05$. (**E**) Individual NHP values upon PC1 and PC2 drawing two clusters segregating animals injected 24 months before from the others. (**F** and **G**) Network analysis of proteins under the 5th and above the 95th percentile of the PC2 ($n = 300$).
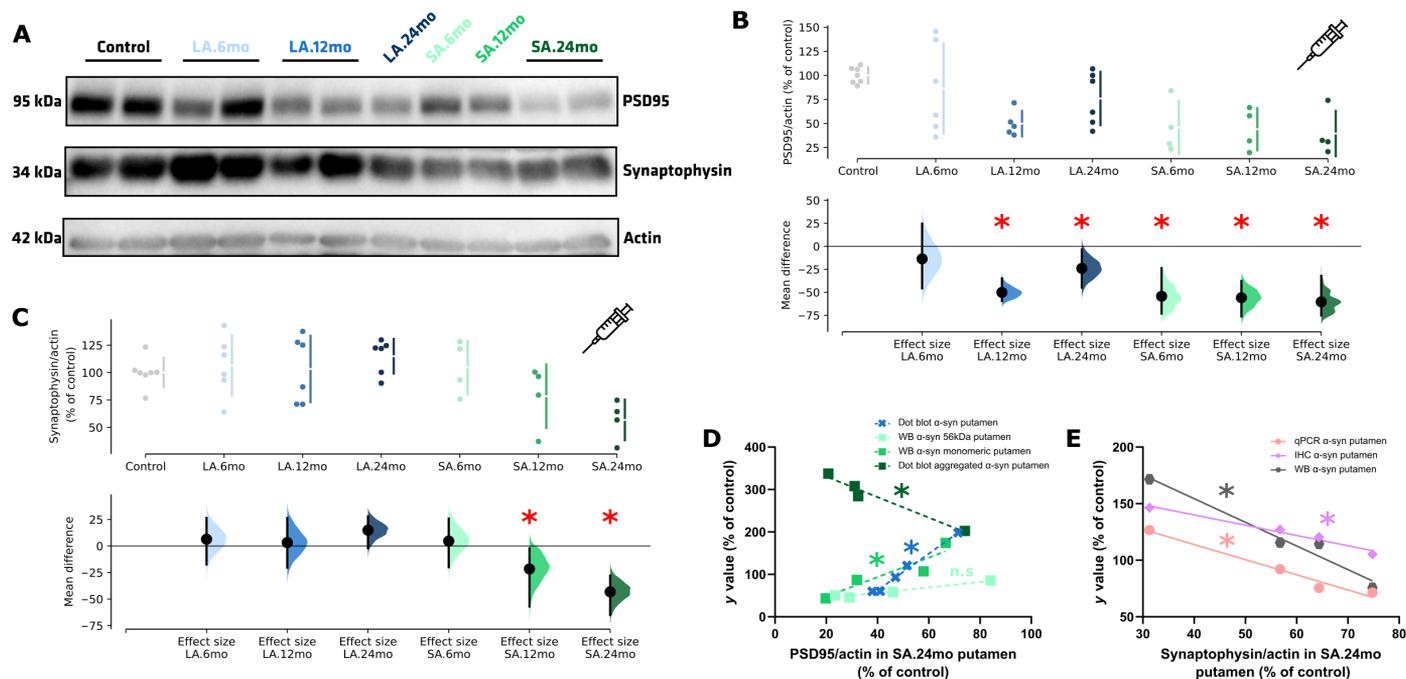
Fig. 6. Biochemical and histological analysis of pre- and postsynaptic proteins. (**A** to **C**) Illustrative images (A) and scatter plots (B and C) of immunoblot analysis of postsynaptic protein (B) PSD-95 and (C) synaptophysin in the putamen of controls and LA- and SA-injected NHPs. (**D**) Correlation between PSD-95 immunoblot data and α-syn dot blot in LA.12mo ($R^2 = 0.9944$, $P = 0.0005$), 56-kDa α-syn immunoblot in SA.6mo ($R^2 = 0.9576$, $P = 0.0214$), monomeric α-syn immunoblot in SA.12mo ($R^2 = 0.9235$, $P = 0.0765$), and aggregated α-syn dot blot in SA.24mo ($R^2 = -0.9817$, $P = 0.0183$). (**E**) Correlation between synaptophysin immunoblot levels and α-syn levels in the putamen as measured by qPCR ($R^2 = -0.9862$, $P = 0.0138$), immunohistochemistry (IHC) ($R^2 = 0.9865$, $P = 0.0135$), and immunoblot ($R^2 = -0.9815$, $P = 0.0185$) in the SA.24mo group. Data are expressed as means ± SD, and the bootstrapped mean difference with 95% CI (error bar) is shown on the bottom part of the graph. Statistical analysis was performed using the two-sided permutation t test. *$P < 0.05$ compared to control animals. WB, Western blot.

the onset of synucleinopathy in the putamen, or at least the consequences thereof. On the other hand, the down-regulation of synaptophysin expression in the SA.24mo group (Fig. 6E) negatively correlated with the expression of α-syn in the putamen, as revealed by quantitative polymerase chain reaction (qPCR; $R^2 = -0.9862$, $P = 0.0138$), immunoblot ($R^2 = -0.9815$, $P = 0.0185$), and immunostaining in the putamen ($R^2 = 0.9865$, $P = 0.0135$). This indicates that the increase of α-syn is associated with a decrease of synaptophysin expression levels in the putamen. Together, these findings support the relevance of our proteomic results and indicate that synaptic disorganization preferentially affects the SA groups compared to the LA groups.

LA induces complex reorganization of mitochondrial activity in entorhinal cortex
Proteomic analysis of the entorhinal cortex highlighted differences in several mitochondria-related proteins between the LA and SA groups. To determine the potential mechanisms underlying mitochondrial alterations in the entorhinal cortex, we next analyzed translocase of the outer mitochondrial membrane complex subunit 20 (TOM20) expression as a marker of mitochondrial mass due to its constitutive expression in the outer mitochondrial membrane (OMM) (23) and the two splicing forms of OPA1, namely, the short (S-OPA1) and the long (L-OPA1) forms. S-OPA1 is involved in restoring energetic efficiency (24), while L-OPA1 is mostly involved in mitochondrial fusion. Long and short forms of OPA1 complement each other to reconstitute mitochondrial morphology.
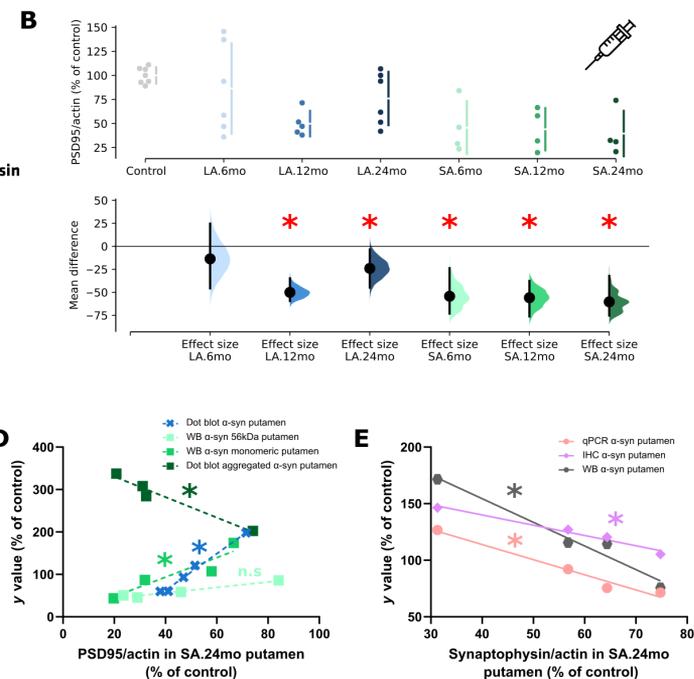
Immunoblot analysis of TOM20 revealed an opposite change in expression in the LA.24mo group (213.1% of control) and the SA.24mo group (45.3% of control) (Fig. 7A). TOM20 distribution was further assessed by immunofluorescence. No alterations were found in the LA groups. However, in the SA groups, a significant increase of TOM20 total surface was observed at 6 months (+14.9 μm² per cell) followed by a decrease at 12 months (−20.5 μm²) and 24 months (−13.9 μm²) (Fig. 7B), demonstrating a progressive reduction in mitochondrial mass in the entorhinal cortex.

Further supporting the occurrence of mitochondrial alterations, we quantified the different OPA1 isoforms by immunoblot analysis (Fig. 7C). This method accurately depicts subtle changes in mitochondrial morphology, motility, and energy production (25–27). In the LA groups, S-OPA1 immunoblot levels were significantly decreased (−36.24%) only in the LA.24mo group compared to that in the control group (Fig. 7D), which might suggest a late mitochondrial energy deficit. This S-OPA1 decrease tends to correlate with histological pSyn assessment in the entorhinal cortex ($R^2 = 0.6552$, $P = 0.051$) (Fig. 7E). We observed that L-OPA1 significantly rose in the LA.12mo (+145.8%), SA.6mo (+142.5%), and SA.24mo (+133.8%) groups compared to that in controls, suggesting an enhanced mitochondrial fusion (Fig. 7F). Overall, the results obtained in the LA groups indicate several mitochondrial alterations, including an increase in mitochondrial mass associated with a loss of energy efficiency at 24 months, likely due to an enhancement of mitochondrial fusion at 12 months. In the SA group, the results suggest mainly a progressive loss of mitochondrial mass.
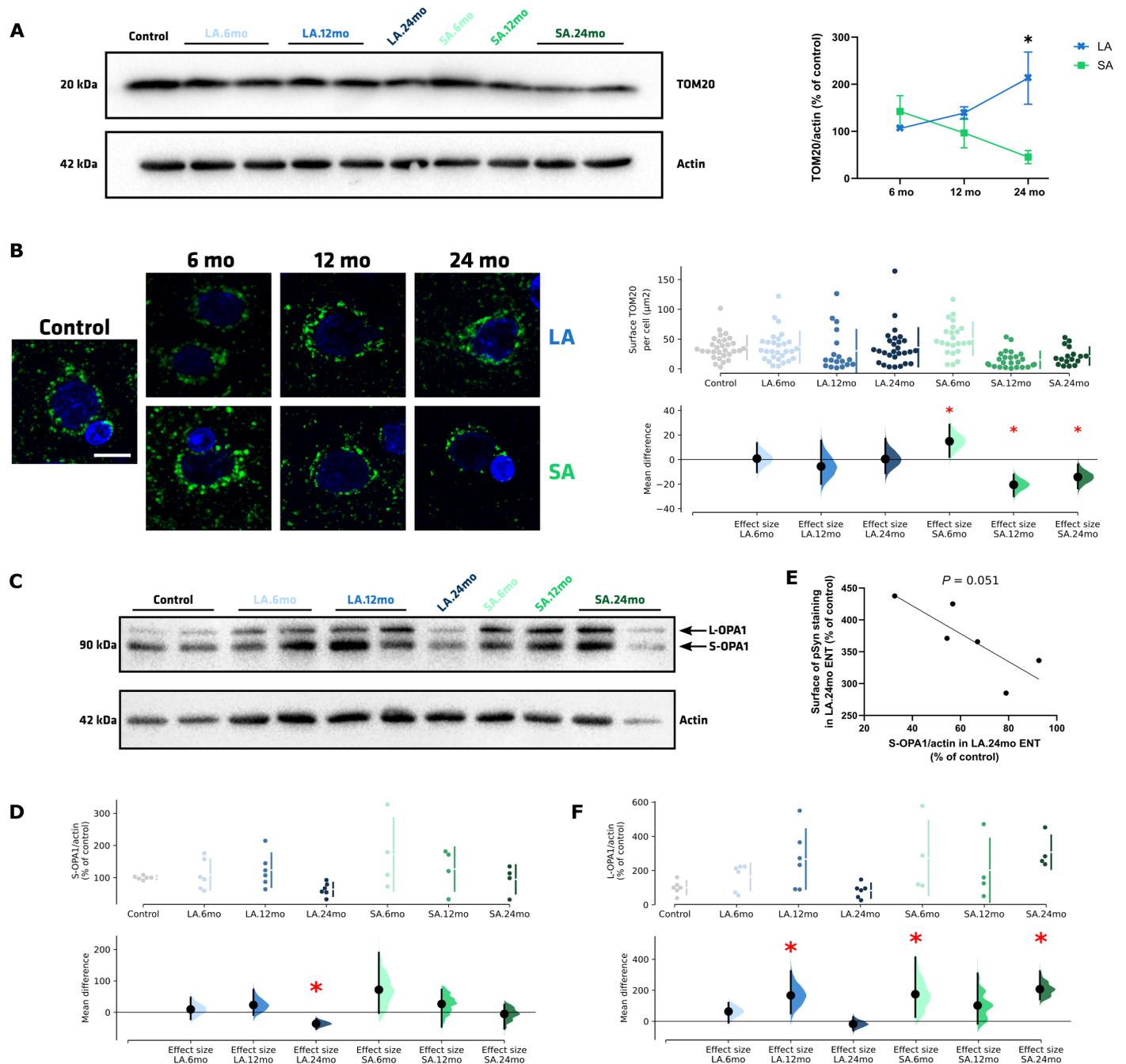
Fig. 7. Biochemical and histological analyses of mitochondrial markers reveal changes in dynamics between LA and SA groups. (**A** and **B**) Immunoblot of TOM20 (A) and TOM20 immunofluorescence staining (B) analyses in the different experimental groups in the entorhinal cortex. Scale bar, 5 μm. (**C** to **F**) Entorhinal cortex (ENT) immunoblot analysis of internal mitochondrial membrane protein OPA1, including the short (S-OPA1) (D) and the long (L-OPA1) (F) forms, displaying a correlation between S-OPA1 and with pSyn IHC level in the LA.24mo group ($R^2 = 0.6552$, $P = 0.051$) (E). Data are expressed as means ± SD, and the bootstrapped mean difference with 95% CI (error bar) is shown on the bottom part of the graph. Statistical analysis was performed using a two-sided permutation t test. *$P < 0.05$ compared with control animals. mo, months.

DISCUSSION

Here, we shed light on the complexity of the pathology induced by SA and LA forms of α-syn–enriched PD patient–derived fractions. We identified differential kinetics and mechanisms associated with the injection of SA and LA by performing an in-depth longitudinal characterization in a large NHP cohort. Using proteomics, we highlighted the shared and unique cellular responses associated with small or large α-syn aggregates. We observed that pre- and postsynaptic changes depend on the fraction type. Also, mitochondrial alterations were observed in the entorhinal cortex, with a decreased mitochondrial mass in the SA groups and a mitochondrial complex activity reorganization in the LA groups.

Relying on our extensive pathological characterization covering 180 behavioral, histological, and biochemical parameters applied to 40 brain areas of interest combined with an unbiased comparative proteomics approach, we gained insight into a comprehensive mapping to elucidate the temporal and spatial pathological changes induced by two distinct PD patient–derived α-syn pathogenic structures (14). We previously showed that small (SA) and large (LA) α-syn assemblies induce dopaminergic degeneration in NHPs 2 years after administration (14) without knowing (i) the precise kinetics of those neurodegenerative changes and (ii) the putative differential pathological pathways involved. This longitudinal study shows that the dopaminergic axonal depletion in the caudate nucleus appears early (i.e., at 12 months) in the LA-injected group (Fig. 1H), demonstrating an early pathological effect of highly enriched aggregated α-syn fractions. This suggests a major impairment in the organization of the nigrostriatal projections, affecting consequently the dopaminergic cells located in the dorsal part of the SN, which project to the caudate nucleus (18, 28). Early dopaminergic depletion in the caudate nucleus correlates with the onset of cognitive symptoms such as depression and gait problems, reported in the literature (29) but not in our study, possibly because the striatal dopaminergic terminal loss in the caudate nucleus remained below the threshold of overt symptom appearance (~50% of terminal loss) (30, 31).

To monitor pathological pseudo-progression, we quantified the regional burden of α-syn pathology at each time point, measuring pSyn as a surrogate marker. We observed an earlier rise of pSyn in the LA groups compared to that in the SA groups in multiple brain regions (Fig. 2C), except for the lateral dorsal nucleus of the thalamus, preferentially linked to behavioral impairment in patient with PD, such as freezing of gait (32). These findings reinforce the view that LA (Fig. 3E) and SA (Fig. 3F) may activate distinct pathogenic processes and dynamics over time, a concept developed in our earlier study using a machine learning–based approach (14). This approach echoes a longitudinal study using striatal injections of α-syn preformed fibrils in mice between 2 weeks and 18 months. This study used whole-brain tissue clearing, high-resolution imaging, and a computational model for tracking both the origin and the propagation pathways of pSyn pathology from the striatum through multiple retrograde routes in the cortico-basal-ganglia-thalamo-cortical loop (33), emphasizing that anatomical connectivity seems to be the main driver of α-syn spread, in agreement with others (34, 35).

In this context, our study provides an invaluable NHP dataset for a better understanding and characterization of the pathogenic processes induced by the putaminal injection of small, mostly soluble, α-syn extracts (i.e., SA) or large, mostly aggregated, α-syn extracts (i.e., LA) derived from patient with PD. Recent research has revealed that more than one species of amyloid is present in neurodegenerative disease brains, including PD (36, 37), where small non-fibrillar α-syn aggregates are the critical species driving neuroinflammation and disease progression (38). The presence of different amyloid structures allows to speculate that individual fibril conformations dictate different disease conditions, significantly complexifying any attempt at disease modeling. In the present study, we have identified at least two families of species derived from the same PD brains, named LA and SA, which are two distinct brain-derived amyloids based on the evidence of micro-infrared spectroscopy (14). We have demonstrated that each type of amyloid is associated with unique and specific pathological pathways (SA is linked to synaptic dysfunction, while LA is linked to mitochondrial reorganization and dysfunction). Despite their different mechanisms, both amyloids ultimately result in similar behavioral abnormalities, as predicted by comparable nigrostriatal denervation. Only a study on NHPs has the power to unravel this behavior, as mice are not sensitive to SA (14). This study suggests that patients likely harbor different amyloids that trigger distinct pathogenic pathways, converging to the same nigrostriatal damage.

Our study included an unbiased exploration of the proteome of two selected brain regions, locally or remotely, affected by LA and SA. Proteomic analysis of the injection site (i.e., putamen) allowed us to discriminate protein clusters, explaining most of the differences between experimental groups focusing on the synaptic network (Fig. 4F). To confirm the involvement of this pathway, we determined the expression of synaptophysin and PSD-95, validated pre- and postsynaptic markers, respectively, through immunoblot and immunofluorescent techniques. We show a synaptic network remodeling after 1 year in LA-injected animals, with the decreased levels (Fig. 6B) of PSD-95 correlating with the protein folding status of α-syn in the putamen (Fig. 6D), along with the decrease in presynaptic synaptophysin elements (Fig. 6E). Our results are reminiscent of other in vivo and human postmortem studies showing that dopaminergic depletion decreases PSD-95 levels in the striatum (39) due to accumulating presynaptic α-syn aggregates (40). In addition, we observed a progressive decrease in striatal TH-positive dopaminergic fibers, which became significantly pronounced earlier in LA-injected compared to SA-injected animals (Fig. 1, G and H). This decrease positively correlates with the increase in pSyn levels in the putamen (fig. S2F) as well as in the caudate nucleus (fig. S2G), potentially explaining the progressive postsynaptic changes observed in the different experimental groups. This is in line with evidence that overexpression of α-syn decreases synaptic vesicle motility in neurons (41, 42) and that elevation in α-syn concentration causes the clustering of synaptic vesicles (43). Furthermore, a longitudinal cerebrospinal fluid (CSF) biomarker study performed in patient with de novo PD showed a decrease in synaptic and neuroplasticity markers, such as pentraxins, and a correlation with cognitive impairment (44).

We also conducted a proteomic analysis of the entorhinal cortex, a known site for major α-syn pathology burden in this model (Fig. 2C) (14). Such analysis allowed us to unmask predominantly mitochondrial alterations in this area following PD patient–derived fractions injection. The proteins explaining most of the PC2 variance, which discriminates between control and animals receiving patients-derived fractions at 6 months from those receiving it at 12 and 24 months (Fig. 5D), were mainly linked to oxidative phosphorylation processes (Fig. 5F). Mitochondrial dysfunction has

long been considered an important pathogenic factor in PD (45). Mitochondrial alterations following the use of α-syn–derived material have been demonstrated in mice injected with preformed fibrils, leading to a decrease in mitochondria complex I activity, an increase in oxidative stress, and cell death (46). Here, we show a different and opposite pattern between the LA and SA groups at the latest time point concerning both the mitochondrial mass (Fig. 7A) and the cell surface occupied by TOM20 (Fig. 7B). This result indicates an impact of α-syn pathology on mitochondrial function and activity. Such impact has been previously recognized through the demonstration that mutant α-syn aggregates in mitochondria and subsequently alters mitochondrial function, ultimately leading to toxicity (47). Adeno-associated virus (AAV)–mediated TOM20 overexpression has been shown to prevent α-syn–induced dopaminergic depletion in a PD rat model overexpressing wild-type α-syn (48) and, hence, proposed as a therapeutic strategy. We investigated OPA1, a mitochondrial fusion protein with a role in cristae shaping (24). Disruption of OPA1 causes mitochondrial dysfunction (49). We show that OPA1 (and its splice variant) is affected over time, but only in the LA groups. The long form anchored to the inner mitochondrial membrane (IMM) mainly regulates mitochondrial morphology and fusion. In contrast, the short form plays a role in the energetic functions of the mitochondria (50). Our data revealed mitochondrial structural alterations at 12 months (Fig. 7F), which led to a drop in mitochondrial energy at 24 months (Fig. 7E), as evidenced by S-OPA1. This drop negatively correlates with pSyn accumulation (Fig. 7F), indicating that the increase in pSyn is associated with a decrease in the soluble form of OPA1, which is also associated with a protective role in oxidative stress, improving cell survival. The TOM complex has been identified as a potential passive α-syn transporter through the OMM (51). α-Syn and pSyn are known to colocalize and interact with TOM20 (52), disrupting its interaction with TOM22 and leading to mitochondrial protein import damage (53). Hence, OPA1 dysregulation in the LA groups at 6 and 12 months may cause the rise of TOM20 expression at 24 months, facilitating IMM dysregulation by α-syn. A recent gene set enrichment analysis in patients with idiopathic PD revealed, on the one hand, a decrease in mitochondrial and bioenergetic processes and, on the other hand, greater mitochondrial alterations in patients with more severe motor symptoms (44).

Synaptic and mitochondrial deficits have been reported in postmortem PD brains. Transcriptomic analysis of pSyn-positive versus pSyn-negative neurons revealed a significant down-regulation of synapse- and mitochondria-related genes (54). Moreover, the same type of analysis in mice injected with α-syn preformed fibrils also showed a decrease in synaptic and mitochondrial gene expression (54), supporting our findings in NHPs regarding the dysregulation of these fundamental cellular mechanisms.

Our study has several limitations and areas that require further clarification. First, an objection might be raised regarding the control group not receiving any stereotaxic injection compared to the SA and LA groups. This investigation is part of a larger program studying the synucleinopathies in a large baboon colony living in an aviary, where some received not only putaminal injection (14), as described here, but also cortical injection (16) and enteric injection (15) of PD-patient derived fractions. Before these studies, only two reports have established synucleinopathy models in olive baboons (55, 56). Consequently, it was necessary to establish basic parameters, such as the number of TH-positive cells in the SNpc or other dopaminergic and α-syn–related data. Considering these factors, the non-injected control group was deemed the most appropriate for our study. Another limitation may be that the potential synergy between these α-syn assemblies and their effects on other brain structures involved in PD pathogenesis, such as the SN, raphe nuclei, or olfactory nucleus, remains to be explored. This could uncover different cellular pathway impairments, highlighting the need for future studies. For example, varying the injection sites of patient-derived fractions may influence pathogenic outcomes, as demonstrated by the enteric administration of LA fractions in baboons (15).

From a translational perspective, developing more precise and effective treatments hinges on a detailed understanding of the distinct amyloid species involved and/or the pathogenic pathways activated. Our study unequivocally demonstrates that different α-syn species or aggregates of different sizes that coexist in the PD brain led to PD-like pathology. Identifying the different strains will contribute to define the biological subtypes of PD and guide the selection of therapeutic strategies, including immunization, small molecules targeting α-syn, aggregation inhibitors, and clearance enhancers. These findings could uncover previously unidentified therapeutic targets and offer the potential for precision medicine approaches, with diagnostic tools designed to distinguish and target different pathogenic entities in living patients.

MATERIALS AND METHODS
Ethics statement
Experiments were performed in accordance with the European Union directive of 22 September 2010 (2010/63/EU) on the protection of animals used for scientific purposes. The Institutional Animal Care and Ethical Committee of Murcia University (Spain) approved experiments under the license number REGA ES300305440012.

Purification of α-syn aggregates from human PD brains
α-Syn aggregates purification was conducted as previously described (13–16, 57). The data reporting the complete characterization of α-syn–derived fractions used for the injections were not included in this study but in our previous publication (14). The samples were obtained from brains collected in a Brain Donation Program of the Brain Bank "GIE Neuro-CEB" run by a consortium of Patients Associations: ARSEP (association for research on multiple sclerosis), CSC (cerebellar ataxias), France Alzheimer, and France Parkinson. The consent forms were signed by the patients themselves or their next kin in their name, following the French Bioethical Laws. The Brain Bank GIE Neuro-CEB (Bioresource Research Impact Factor number BB-0033–00011) has been declared at the Ministry of Higher Education and Research and has received approval to distribute samples (agreement AC-2013–1887). Fresh-frozen postmortem midbrain samples from five patients with sporadic PD, who exhibited noticeable nigral LB pathology upon neuropathological examination, were dissected (mean age at death, 75 ± 2.75 years; frozen postmortem interval, 31.8 ± 7.45 hours; GIE Neuro-CEB BB-0033–00011). Briefly, tissue was homogenized in 9 volume (w/v) of ice-cold MSE buffer [10 mM Mops/KOH (pH 7.4), 1 M sucrose, 1 mM EGTA, and 1 mM EDTA] with a protease inhibitor cocktail (cOmplete Mini, Boehringer Mannheim) using a motor-driven glass/Teflon dounce homogenizer for 12 strokes. For α-syn aggregates purification, a sucrose step gradient was prepared by layering 2.2, 1.4, and, lastly, 1.2 M sucrose in volume ratios of 3.5:8:8 (v/v). The homogenate was placed

on the gradient and centrifuged at 160,000*g* for 3 hours using a SW32.1 rotor (Beckman). Twenty-six fractions of 1500 μl each were collected from each gradient from top (fraction 1) to bottom (fraction 26) and analyzed for the presence of α-syn aggregates by filter retardation assay, as previously described (*14*). Further LB fractions were characterized further by immunofluorescence, α-syn ELISA quantification, and electron microscopy as previously described (*14*). For stereotactic injections, LB-containing fractions from patient with PD were combined in the same proportion (PD#1, fractions 19 and 20; PD#2, fractions 19 and 20; PD#3, fraction 22; PD#4, fractions 17, 18, and 19; and PD#5, fractions 20, 21, and 23). NoLB-containing fractions (i.e., fraction 3, at the beginning of the 1.2 M interface) derived from the same patient with PD (which contain soluble or finely granular α-syn but lack large LB-linked α-syn aggregates) were obtained from the same sucrose gradient purification. The amount of α-syn in the LB fractions was quantified using a human α-syn ELISA kit (no. KHB0061, Invitrogen/Life Technologies, Carlsbad, CA, USA) and is reported in (*14*). Briefly, α-syn concentration was measured, and both LB and noLB fractions were adjusted to 24 pg α-syn per microliter. We used the same SN-derived LB fractions for all the experimental groups in this large-scale study, i.e., striatum-, ENS-, and cortex-injected animals. Those SN-derived LB fractions have been fully characterized biochemically (*14*) and demonstrated their ability to induce neurodegeneration and α-syn pathology after either striatal [reminiscent of our princeps article; (*13*)] or gut injections. In all cases, samples were bath-sonicated for 5 min before in vivo injections. Of note, in this article, we felt it would be more appropriate and accurate to modify the nomenclature to better understand the pathological consequences of our results. LB and noLB fractions have been renamed by LA and SA, respectively.

Electron microscopy
Briefly, carbon-coated nickel grids were covered for 1 min with corresponding fractions of interest and then washed three times with distilled water. They were then washed again in distilled water and stained for 5 min with 2% uranyl acetate before being air-dried. Digital images were obtained with a computer linked directly to a charge-coupled device camera (Gatan) on a Hitachi H-7650 electron microscope. LA samples were bath sonicated for 5 min before the in vitro applications in the same condition as in vivo procedure. The length of amyloid fibrils and their fragments was manually measured through the ImageJ program.

Atomic force microscopy
AFM micrographs were acquired in the air on AFM 5500 Keysight in tapping mode from samples deposited on clean silicon wafers. Silicon tips from Bruker were used with a fundamental frequency of 150 kHz and a spring constant of 5 N/m. The scan speed was between 0.2 and 0.4 ln/s. The LA images have 512×512 points per line, and the SA images have 262×256 points per line. The data were processed with Gwyddion 2.67. Silicon wafers (1 cm by 1 cm) were cleaned by sonication with isopropanol and rinsed with Milli-Q water. Last, samples diluted with water to a concentration of 0.4 μg/μl were deposited by drop casting (2 min) and posterior spin coating [2 min at 60 revolutions per second (rps)].

Animals and stereotactic injections
Animals were bred and housed in two multi-male, multi-female exterior pens (Animal Facility of the University of Murcia, Murcia, Spain). They were studied in this environment over 2 years. Animals were fed fruits, vegetables, and monkey pellets twice daily before 9:00 a.m. and after 5:00 p.m. Water was available ad libitum. Thirty-seven healthy adult olive baboons (*P. papio*) (21 male and 16 female) were used in this study to reach statistically significant numbers while complying with 3R policy: young (1 to 3 years old, $n = 7$), adult (3 to 7 years old, $n = 11$), mature (7 to 14 years old, $n = 11$), and aged (20 to 22 years old, $n = 8$). Group sizes were chosen, assuming a one-tailed α of 0.05, with a sample size of at least four per group, which provided >80% power to detect a difference between the treatment groups and the control group, using a Fisher's exact test.

Animals were randomized into treatment or control groups. Eighteenth baboons were used for LA injections, 12 for SA injections, and 7 for untreated control animals. Intrastriatal injections of either LA or SA fractions were performed at two rostrocaudal levels of the motor striatum (anterior commissure, −1 and − 5 mm) under stereotactic guidance as previously described (*58*). The total injected volume per hemisphere was 100 μl (two injection sites with 50 μl each at 3 μl/min at each location site). After each injection, the syringe was left in place for 10 min to prevent leakage along the needle track. Several parameters were monitored during the 2-year study, including survival and clinical observations. Animals were monitored regularly following recovery from surgery and euthanized ($n = 6$ for LA and SA $n = 4$) at various predetermined time points (6, 12, or 24 months after injection) with pentobarbital overdose (150 mg/kg, intravenously), followed by perfusion with room temperature 0.9% saline solution (containing 1% heparin) in accordance with accepted European Veterinary Medical Association guidelines.

Immediately after death, the brains were extracted. Each brain was then split along the midline, and each half was further divided into three sections. The left half was promptly frozen by submerging it in isopentane at −50°C for a minimum of 5 min and then stored at −80°C. The right half was preserved for a week in a solution of 4% paraformaldehyde at 4°C, with a volume to tissue ratio of 10. It was then cryoprotected in two consecutive gradients of 20% and then 30% sucrose in phosphate-buffered saline (PBS) before being frozen by submerging it in isopentane at −50°C for at least 5 min. It was then stored at −80°C until it was sectioned. CSF and blood samples (plasma, serum, and whole blood) were meticulously gathered from the 17 animals before euthanasia.

Histological analysis
Extent of lesion
To evaluate the integrity of the nigrostriatal pathway, an immunohistochemistry procedure for TH was carried out on sections of the SNpc and striatum. In brief, free-floating sections of 50 μm from a representative level of the striatum (anterior, medial, and posterior) and serial sections (1 of 12) corresponding to the entire SNpc were incubated with a mouse monoclonal antibody against human TH (1:5000; Millipore, MAB318) overnight at room temperature. This was then revealed by an anti-mouse peroxidase EnVision system (Dako, K400311) followed by 3,3′-diaminobenzidine (DAB) visualization. The free-floating SNpc sections were then mounted on gelatinized slides, counterstained with a 0.1% solution of cresyl violet, dehydrated, and coverslipped. The striatal sections were simply mounted on gelatinized slides and coverslipped. The extent of the lesion in the striatum was quantified by measuring the optical density. The sections were scanned using an Epson expression 10000XL high-resolution scanner, and the images were analyzed using ImageJ open-source software to compare the gray level in each region of interest, namely, the caudate nucleus and putamen. TH-positive

cells in the SNpc were counted blindly with respect to the experimental condition using a motorized Leica DM6000B microscope in conjunction with Mercator software (ExploraNova, France). The SN was outlined for each slide, and probes for stereological counting were applied to the resulting map (probe size was 100 μm by 80 μm spaced by 600 μm by 400 μm). Each TH-positive cell with its nucleus included in the probe was counted. The optical fractionator method was ultimately used to estimate the total number of TH-positive cells in the SNpc of each monkey hemisphere. Additionally, we measured the Nissl cell count, the volume of the SN, and the surface occupied by TH in the SN to comprehensively characterize the pattern of dopaminergic cell loss in the SN. The "surface" is an additional quantification method used in tissue sections. For these analyses, a specific staining process was used to keep all tissues together in the same solution during the staining process. Then, high-resolution whole-color slide images were first acquired with the three-dimensional Histech Panoramic Scanner at ×20 magnification, with five layers in extended mode. Each image was opened using the offline MERCATOR PRO 7.12.3 software (Explora Nova, France), and all regions of interest were mapped. Brightness and contrast rules were applied to the red, green, and blue (RGB) pictures to optimize details without any image saturation. The color thresholding tool was then used to select the threshold corresponding to the brown color revealed by the DAB staining. The threshold was established on the basis of the staining intensity to detect the maximum DAB staining. The file of the threshold parameters was saved and applied to all measurements for each animal/staining. Before performing the quantification, the threshold was randomly applied to some images of different treatment groups to verify the accuracy of the settings. In each region, the software extracted the surface corresponding to the threshold defined. The surface parameter was lastly expressed as a ratio of the total surface of each area of interest.

α-Syn pathology

The evaluation of synucleinopathy was carried out using a mouse monoclonal antibody that was developed against human α-syn (syn211) and phosphorylated α-syn (1:5000; clone 11A5, Elan) (59–66). In brief, chosen sections at two rostro-caudal levels were incubated in the same well to enable a direct comparison of the intensity of the immunostaining. These sections were left to incubate overnight at room temperature with the antibodies mentioned above. The next day, the revelation was carried out with an anti-specie peroxidase EnVision system (Dako), followed by an incubation with DAB. The sections were then mounted on gelatinized slides, dehydrated, counterstained if required, and coverslipped for further analysis. The quantification of the gray level or the surface quantification of the immunostaining-positive areas in 40 brain regions (Fig. 2B) was carried out after NanoZoomer 2.0 HT scan and analyzed with Mercator software (ExploraNova, La Rochelle, France). In brief, the different regions were outlined, and a consistent color threshold was applied to all images to ensure comparability across experimental groups. The area detected relative to the threshold was then measured. The ratio of the total area of interest to the thresholded area was lastly used to determine the percentage of the syn/pSyn-stained structure within the area of interest (67). The z-score was calculated from the control group's mean and SD for each staining of every region. Then, the control group's mean was subtracted from the experimental group's mean and divided by the SD of the control group. Briefly, first, we normalized every group and time

point to our reference group by dividing individual values by the control means. Then, we expressed their "fold changes" as a z-score by subtracting the SD and dividing by the overall mean.

Mitochondrial markers

Sections were permeabilized for 1 hour in a 4% donkey serum/PBS blocking buffer containing 0.3% Triton X-100 (MilliporeSigma) and incubated overnight at 4°C with a rabbit polyclonal antibody raised against TOM20 (1:500; 11802-1-AP, Proteintech) diluted in a 1% donkey serum/PBS buffer. Following incubation with primary antibodies, tissues were washed with PBS three times for 10 min and incubated for 1.5 hours at room temperature with a donkey anti-rabbit coupled to an Alexa Fluor 488 (1:200; A-21206, Invitrogen). Slices were treated with Sudan Black B 0.1% in ethanol 70% to reduce autofluorescence before slide mounting, and confocal observation with Leica DMI6000 TCS SP8 X at 63× oil magnification was performed.

Biochemical analysis

Total protein extraction and quantification

Immunoblot analyses were conducted on the putamen and entorhinal cortex. Five tissue samples were extracted on ice using 100 μl of radioimmunoprecipitation assay (RIPA) buffer [50 mM tris-HCl (pH 7.4), 150 mM NaCl, 1.0% Triton X-100, 0.5% Na-deoxycholate, and 0.1% SDS] along with a protease inhibitor cocktail tablet (cOmplete Mini, Roche Diagnostics). The lysate was chilled on ice for 20 min before being centrifuged at 14,000 rpm for 15 min at 4°C. The supernatant was then collected, and the total protein content in the lysates was determined using the bicinchoninic acid (BCA) Assay. The samples were subsequently stored at −80°C. Using the total protein concentrations determined from the BCA assays, aliquots of tissue lysates, which correspond to specific amounts of total protein per lane, were prepared for each animal. These preparations were made in Laemmli buffer (containing 25 mM tris-HCl with a pH of 6.8, 7.5% glycerol, 1% SDS, 250 mM dithiothreitol, and 0.05% bromophenol Blue) for the purpose of conducting an immunoblotting experiment.

Western blot analysis

Western blots were conducted under all conditions using 20 μg of protein that was separated by SDS–polyacrylamide gel electrophoresis (PAGE) and then transferred to nitrocellulose. The primary antibodies were incubated overnight at 4°C with rabbit anti-OPA1 (1:1000; 27733-1-AP, Proteintech), rabbit anti-TOM20 (1:1000; 11802-1-AP, Proteintech), and anti–α-syn (phospho-S129) (1:1000; EP1536Y, Abcam) (68), and mouse anti–β-actin (1:10,000, A5441, Sigma-Aldrich) was used to ensure equal loading. Suitable secondary antibodies linked to peroxidase were revealed using a Super Signal West Pico Chemiluminescent kit (Immobilon Western, Chemiluminescent HRP substrate, Millipore). Chemiluminescence images were captured using the ChemiDoc+XRS system measurement (Bio-Rad). The signals for each lane were quantified using ImageJ, and a ratio of signal on loading per animal was calculated and used in statistical analyses. Synaptic markers analysis followed the same protocol, adding citrate antigen-retrieval step pH 6 (S1699, Dako) on the nitrocellulose membrane before using rabbit antibody raised against PSD95 (1:1000; AB18258, Abcam) and mouse anti-synaptophysin (1:500; AB8049, Abcam).

Variable analysis

Behavioral assessment

Baboon behavior was monitored outside of feeding and cleaning periods for 4 to 9 days (eight sessions per group), in a random order at

two time points (morning and afternoon), after a minimum 4-hour habituation phase that was completed 1 day before the start of the observations. The habituation phase took place across 3 days on the first observational time point, which is 1 month after surgery, enabling the observer to identify each animal separately. During 2-hour sessions, we examined behavioral parameters every 5 min using a scan sampling method that is suitable for time budgeting (69), yielding 192 scans per subject. To prevent missing data, additional observational sessions were carried out. At the two study time points, 1 month and 24 months after surgery, a single trained observer [SC (Sandrine Camus); intraobserver reliability, Spearman rank-order correlation coefficient (r) = 0.987] recorded the data in real time. The distance between the observer and the outdoor cages was 1 m. Instead of concentrating on individual things, we used two repertoires, which, in accordance with published methods (70–72), reflect the interaction with the environment and describe the position within it. The percentages of each item's recurrence in relation to the total number of scans were examined to derive location profiles, body orientation, and mean behavioral and postural time budgets.

Quantitative polymerase chain reaction

After homogenizing SN samples in TRI reagent (Euromedex, France), RNA was extracted following a conventional chloroform/isopropanol procedure. RNA was prepared and examined using modified procedures (56). Using RevertAid Premium Reverse Transcriptase (Fermentas), oligo(dT), and random primers (all from Fermentas), cDNA was generated from 2 μg of total RNA. A LightCycler 480 Real-Time PCR System (Roche, Meylan, France) was used to carry out the qPCR. For every sample, two qPCRs were run in duplicate using transcript-specific primers, 4 ng of cDNA, and a final volume of 10 μl of LightCycler 480 SYBR Green I Master (Roche). The NeuroCentre Magendie developed the Gene Expression Analysis Software Environment, an informatics application that was used to export and evaluate the PCR data. The reference gene was identified using the geNorm approach. The analysis of relative expression was normalized against two reference genes and adjusted for PCR efficiency. The reference genes used were eukaryotic translation initiation factor 4a2 (EIF4A2) and proteasome subunit beta type 6 (Psmb6). The comparative ($2 - \Delta\Delta Ct$) approach was used to compute the relative expression level. The primer sequences are as follows: SNCA (CR457058), GGGCAAGAAT-GAAGAAGGAGC (forward) and GCCTCATTGTCAGGATCCACA (reverse); Psmb6 (NM_002798), CAAGAAGGAGGGCAGGTG-TACT (forward) and CCTCCAATGGCAAAGGACTG (reverse); and EIF4a2 (NM_001967), TGACATGGACCAGAAGGAGAGA (forward) and TGATCAGAACACGACTTGACCCT (reverse).

Dot blotting analysis of α-syn

This method was used, as we had previously explained (13, 73). Following a 5-min heating period at 100°C, 20 μg of protein extract was diluted using a buffer consisting of 25 mM tris-HCl, 200 mM glycine, and 1% SDS. The mixture was then filtered through an acetate cellulose membrane (Bio-Rad; 0.2-μm pore size) or nitrocellulose membrane. After saturating the membranes in 5% dry-skimmed milk in PBS, antibodies against α-syn (syn211; 1:1000), α-syn fibrils, and α-syn oligomers [Syn-O1; 1:10,000; (74)] were used to probe the membranes (supplied by O. M. A. El-Agnaf). The instructions for the Western blot Analysis section were followed when performing the revelation. Filter retardation assay of SA and LA fractions was probed with antibodies against α-syn (Syn211) recognizing amino acid residues 121 to 125 in both soluble and pathological α-syn (75), phosphorylated α-syn (1:1000; Abcam, EP1536Y),

ubiquitin (1:1000; Sigma-Aldrich, U5379), p62 (1:1000; Progen, GR62-C), hyperphosphorylated tau (AT8; Thermo Fisher Scientific, MN1020), or Aβ (1:1000; clone 6F/3D, Dako), as previously reported in (14).

SR-XRF microscopy

The synchrotron tests were conducted at the Diamond Light Source, Harwell Science and Innovation Campus (Didcot, UK), using 300-mA currents in top-up injection mode and a storage ring with an energy of 3 GeV. The microfocus spectroscopic beamline (I18) was used for all SR-XRF microscopy investigations that are presented in this article. Using a Si(111) monochromator, the micro-XRF elemental mapping was obtained at room temperature with an incident x-ray energy of 12 keV, yielding an x-ray photon flux of 2×10^{11} photons/s. To ensure contamination-free samples and reduced x-ray scattering contribution, the SN of each animal was collected from free-floating sections and mounted onto an x-ray transparent, metal-free, 4-μm-thick Ultralene foil (SPEX CertiPrep, Metuchen, NJ, USA) that was fastened to a custom polyetheretherketone holder. A magnetic plate attached to the sample stage held the samples in place. Operating in the 90° geometry, the four-element Si drift Vortex ME4 energy-dispersive detector (Hitachi High-Technologies Science America) reduces the background signal thanks to its Xspress 3 processing circuits. The 75-mm sample-to-detector distance was fixed. While the XRF spectra were being gathered, the sample was rastered in front of the incident x-ray beam at a 45° angle. Because of the low element concentration, a region of 500 μm by 500 μm within the SNpc was mapped for each sample, with a dwell period of 1 s per pixel and a step size that matches the beam size (5 μm). To calibrate the experimental parameters, a thin-film XRF reference material (AXO DRESDEN GmbH) and a thin (100 μm) pellet of the National Institute of Standards and Technology (NIST) standard reference materials SRM1577c (bovine liver material, NIST, Gaithersburg, MD, USA) were assessed. The next step involved quantifying the elements using PyMCA, an open-source software program that models the major composition, density, and thickness of both the sample and the reference material. The elemental concentration (micrograms per gram of dry weight or parts per million) maps were created, the fluorescence spectra acquired from each pixel was fitted, and the average elemental concentration of the SNpc regions was found.

α-Syn in monkey biological fluid samples

The capture antibody MJFR1 (3 μl/ml; Abcam, Cambridge, UK) was coated onto multi-array 96-well plates [Meso Scale Discovery (MSD), Gaithersburg, MD, USA] for an overnight incubation at 4°C without shaking. The following day, 150 μl of PBS-T [PBS (Appli-Chem, Darmstadt, Germany) mixed with 0.05% Tween 20 (Roth, Karlsruhe, Germany)] per well was used to wash the plates three times. The prevention of nonspecific protein binding was achieved through a 1-hour incubation period and shaking at 700 rpm of 150 μl of 1% bovine serum albumin (BSA; SeraCare Life Sciences, Milford, MA, USA)/PBS-T each well. Single-use aliquots of α-syn (1 μg/ml) kept at −80°C until needed were used to construct calibrators (supplied by O. El-Agnaf), which ranged in concentration from 25,000 to 6.1 pg/ml in sequential fourfold dilutions. A blank of 1% of BSA/PBS-T was used. The following dilutions were used for the different specimens: 1 in 8 for serum, plasma, and CSF, and 1 in 10,000 for whole blood. Every dilution was made using 1% BSA/PBS-T. Following plate washing, 25 μl of the calibrator solution and diluted samples were added to the wells, and the incubation period was followed.

After a second washing of the plates, 25 µl of the Sulfo-TAG–labeled Syn1 antibody (BD Biosciences, Heidelberg, Germany) was added to each well as a detection antibody. The antibody was diluted to 1 µg/ml in 1% PBS-T. Using MSD Sulfo-TAG NHS-Ester (MSD), Sulfo-TAG labeling was carried out in accordance with the manufacturer's instructions. The incubation process lasted an hour at 700 rpm. After washing the plates, 150 µl of 2× Read Buffer (MSD) was applied, and an MSD Sector Imager 2400 was used to read the plates. Workbench software was used to analyze the data (MSD).

Neurotransmitter analysis

Brain patches were removed and placed in 1.5-ml Eppendorf tubes after being weighed and dissected on an ice-cold plate. After homogenizing the samples in a 50:50% v/v methanol/water mixture, the samples were centrifuged for 15 min at 4°C at 14,000 rpm. After being separated, the supernatant was kept at −80°C until amino acid derivatization. Following precolumn derivatization with o-phthaldialdehyde/mercaptoethanol (OPA) reagent, the glutamate and GABA content of the samples was determined using high-performance liquid chromatography (HPLC) in conjunction with fluorometric detection (FP-2020 Plus fluorimeter, Jasco, Tokyo, Japan). A refrigerator autosampler maintained at 4°C automatically added 30 µl of OPA reagent to 28 µl of sample (Triathlon, Spark Holland, Emmen, The Netherlands). A 5-C18 Hypersil ODS column (3 mm by 100 mm; Thermo Fisher Scientific, USA) was filled with 50 µl of the mixture, which was then perfused at a rate of 0.48 ml/min (Jasco PU-2089 Plus Quaternary Pump; Jasco, Tokyo, Japan) using a mobile phase that contained 2.2% tetrahydrofuran (pH 6.5), 10% methanol, and 0.1 M sodium acetate. ChromNAV software (Jasco, Tokyo, Japan) was used for the acquisition and analysis of chromatograms. GABA and glutamate had limits of detection of around 1 and 0.5 nM, respectively, and retention periods of ~3.5 and 18.0 min.

Proteomic analysis

Sample processing protocol

Tissue patches from the putamen and the entorhinal cortex were collected on 300-µm-thick cryostat-cut sections ($n = 5$ to 10 patches per structure and animal). Patches were pooled and mechanically lysed on ice with 100 µl of RIPA buffer (50 mM tris-HCl, 150 mM NaCl, 1.0% Triton X-100, 0.5% Na-deoxycholate, and 0.1% SDS) with a protease and phosphatase inhibitor cocktail as previously described. Lysates were incubated for 30 min and then centrifuged at 15,000g for 15 min at 4°C. Supernatants were collected, and the total amount of protein in the lysates was assessed by BCA assay before storage at −80°C. Protein samples were solubilized in Laemmli buffer, and 5 µg per sample were deposited onto SDS-PAGE gel (10% acrylamide) for separation, concentration, and cleaning purposes. After colloidal blue staining, bands were cut out from the gel and subsequently cut in 1 mm–by–1 mm gel pieces. Gel pieces were unstained in 25 mM ammonium bicarbonate 50% acetonitrile (ACN), rinsed twice in ultrapure water, and shrunk in ACN for 10 min. After ACN removal, gel pieces were dried at room temperature, covered with the trypsin solution (10 ng/µl in 50 mM NH$_4$HCO$_3$), rehydrated at 4°C for 10 min, and lastly incubated overnight at 37°C. Samples were then incubated for 15 min in 50 mM NH$_4$HCO$_3$ at room temperature with rotary shaking. The supernatant was collected, and an H$_2$O/ACN/HCOOH (47.5:47.5:5) extraction solution was added to gel slices for 15 min. The extraction step was repeated twice. Supernatants were pooled and dried in a vacuum centrifuge. Digests were lastly solubilized in 0.1% HCOOH.

Nano–liquid chromatography–tandem MS analysis and label-free data analyses

Peptide mixture was analyzed on an Ultimate 3000 nanoLC system (Dionex, Amsterdam, The Netherlands) coupled to an Electrospray Orbitrap Fusion Lumos Tribrid Mass Spectrometer (Thermo Fisher Scientific, San Jose, CA). Ten microliters of peptide digests were loaded onto a 300-µm–inner diameter by 5-mm C18 PepMap trap column (LC Packings) at a flow rate of 10 µl min^{-1}. The peptides were eluted from the trap column onto an analytical 75-mm–inside diameter by 50-cm C18 Pep-Map column (LC Packings) with a 4 to 40% linear gradient of solvent B in 91 min (solvent A was 0.1% formic acid, and solvent B was 0.1% formic acid in 80% ACN). The separation flow rate was set at 300 nl min^{-1}. The mass spectrometer operated in positive ion mode at a 2.0-kV needle voltage. Data were acquired using Xcalibur 4.4 software in a data-dependent mode. MS scans (m/z 375 to 1500) were recorded at a resolution of $R = 120,000$ (at m/z 200) and an automated gain control target of 4×10^5 ions collected within 50 ms. Dynamic exclusion was set to 30 s and top speed fragmentation in higher-energy collisional dissociation (HCD) mode was performed over a 3-s cycle. MS/MS scans with a target value of 5×10^4 ions were collected in Orbitrap with a maximum injection time of 54 ms and a resolution of 30,000 (at m/z 200). Additionally, only +2 to +7 charged ions were selected for fragmentation. Others settings were as follows: no sheath or auxiliary gas flow; heated capillary temperature, 275°C; normalized HCD collision energy of 28%; and an isolation width of 1.6 m/z. Monoisotopic precursor selection was set to peptide and an intensity threshold was set to 2.5×10^4. Data were searched by SEQUEST through Proteome Discoverer 2.5 (Thermo Fisher Scientific Inc.) against a *Papio Anubis* Reference Proteome Set (UniProt 2021-03; 44,721 entries). Spectra from peptides higher than 5000 Da or lower than 350 Da were rejected. The search parameters were as follows: Mass accuracy of the monoisotopic peptide precursor and peptide fragments was set to 10 parts per million and 0.02 Da, respectively. Only b- and y-ions were considered for mass calculation. Oxidation of methionines (+16 Da), methionine loss (−131 Da), methionine loss with acetylation (−89 Da), and protein N-terminal acetylation (+42 Da) were considered as variable modifications, while carbamidomethylation of cysteines (+57 Da) was considered as fixed modification. Two missed trypsin cleavages were allowed. Peptide validation was performed using Percolator algorithm and only "high-confidence" peptides were retained corresponding to a 1% false-positive rate at the peptide level. Peaks were detected and integrated using the Minora algorithm embedded in Proteome Discoverer. Proteins were quantified on the basis of unique peptides intensities. Normalization was performed on the basis of total protein amount. Protein ratios were calculated as the median of all possible pairwise peptide ratios.

Results processing

Proteomic data were processed using Python (Python software foundation v.3.9.7) and its scientific stacks: scipy (v.1.9.3), numpy (v.1.23.4), matplotlib (v. 3.6.2), and seaborn (v. 0.12.1). Only proteins classified as "master protein" (i.e., proteins reviewed in the UniProt database), with more than one unique peptide and not included in a list of contaminant proteins (such as keratin, trypsin, and intermediate filament rod domain-containing protein types), were retained for the data analysis. Proteins that were differentially expressed were chosen on the basis of (i) a *P* value greater than

$-\log_{10}(0.01)$ and (ii) a fold change of 0.5 or more. PCA was conducted using the scikit-learn module after z-score normalization of intensity values. A correlation map between PCA values and neuropathological assessments was created by performing a Pearson correlation between the individual scores in each PC and the individual values of histological analysis. To ensure a consistent interpretation of the results, an outlier CTL-Tau animal was excluded from entorhinal proteomic analyses because of its abnormal profile (completely separated from the other samples in the PCA analysis). The PC further analyzed in the network-type analysis was chosen on the basis of the positive or negative correlation with histological analysis, the percentage of explained variance, the discrimination profile of PC scores between control and experimental groups, and the results obtained in network analysis. Network analysis of PCA results was carried out using Cytoscape (v.3.9.1), ClueGO (v.2.5.9), and CluePedia (v.1.5.9) with the top 10% proteins (below the 5th percentile and above the 95th percentile) contributing the most to the selected PC. The MS proteomics data have been deposited to the ProteomeX-change Consortium via the PRIDE partner repository with the dataset identifier PXD055962.

Statistical analysis

Statistical analyses were performed with the Python DABEST package producing Gardner-Altman estimation plots type (*76*). The raw data are plotted on the upper axes. On the lower axes, mean differences are plotted as bootstrap sampling distributions. Each mean difference is depicted as a dot. Each 95% confidence interval is indicated by the ends of the vertical error bars. Five thousand bootstrap samples were taken; the confidence interval is bias corrected and accelerated. Any P value reported is the probability of observing the effect size (or greater), assuming the null hypothesis of zero difference is true. For each permutation P value, 5000 reshuffles of the control and test labels were performed. Statistical significance is displayed from a two-sided permutation t test, $*P < 0.05$. To analyze treatment and time effect, comparisons were also performed using two-way analysis of variance (ANOVA) through GraphPad Prism 8.0 (GraphPad Software Inc., San Diego, CA).

PCA was performed in Python (Python software foundation v.3.9.7) and its scientific stacks: scipy (v.1.9.3), numpy (v.1.23.4), and matplotlib (v. 3.6.2). Correlations between variables were assessed with Pearson's correlation analysis.

Supplementary Materials

The PDF file includes:
Figs. S1 to S3
Legend for data S1

Other Supplementary Material for this manuscript includes the following:
Data S1

REFERENCES AND NOTES

1. D. J. Surmeier, J. A. Obeso, G. M. Halliday, Parkinson's disease is not simply a prion disorder. *J. Neurosci.* **37**, 9799–9807 (2017).
2. H. Braak, K. Del Tredici, U. Rub, R. A. de Vos, E. N. Jansen Steur, E. Braak, Staging of brain pathology related to sporadic Parkinson's disease. *Neurobiol. Aging* **24**, 197–211 (2003).
3. M. Teil, M. L. Arotcarena, B. Dehay, A new rise of non-human primate models of synucleinopathies. *Biomedicine* **9**, 272 (2021).
4. E. Bezard, M. Teil, M. L. Arotcarena, G. Porras, Q. Li, B. Dehay, Modeling Parkinson's disease in primates. *Cold Spring Harb. Perspect. Med.* **15**, a041612 (2024).
5. M. E. Emborg, S. Y. Ma, E. J. Mufson, A. I. Levey, M. D. Taylor, W. D. Brown, J. E. Holden, J. H. Kordower, Age-related declines in nigral neuronal function correlate with motor impairments in rhesus monkeys. *J. Comp. Neurol.* **401**, 253–265 (1998).
6. G. Porras, Q. Li, E. Bezard, Modeling Parkinson's disease in primates: The MPTP model. *Cold Spring Harb. Perspect. Med.* **2**, a009308 (2012).
7. D. Kirik, L. E. Annett, C. Burger, N. Muzyczka, R. J. Mandel, A. Björklund, Nigrostriatal α-synucleinopathy induced by viral vector-mediated overexpression of human α-synuclein: A new primate model of Parkinson's disease. *Proc. Natl. Acad. Sci. U.S.A.* **100**, 2884–2889 (2003).
8. A. Eslamboli, M. Romero-Ramos, C. Burger, T. Bjorklund, N. Muzyczka, R. J. Mandel, H. Baker, R. M. Ridley, D. Kirik, Long-term consequences of human alpha-synuclein overexpression in the primate ventral midbrain. *Brain* **130**, 799–815 (2007).
9. S. C. Vermilyea, M. E. Emborg, α-Synuclein and nonhuman primate models of Parkinson's disease. *J. Neurosci. Methods* **255**, 38–51 (2015).
10. Y. Niu, X. Guo, Y. Chen, C.-E. Wang, J. Gao, W. Yang, Y. Kang, W. Si, H. Wang, S.-H. Yang, S. Li, W. Ji, X.-J. Li, Early Parkinson's disease symptoms in α-synuclein transgenic monkeys. *Hum. Mol. Genet.* **24**, 2308–2317 (2015).
11. W. Yang, Y. Liu, Z. Tu, C. Xiao, S. Yan, X. Ma, X. Guo, X. Chen, P. Yin, Z. Yang, S. Yang, T. Jiang, S. Li, C. Qin, X. J. Li, CRISPR/Cas9-mediated PINK1 deletion leads to neurodegeneration in rhesus monkeys. *Cell Res.* **29**, 334–336 (2019).
12. F. Cavaliere, L. Cerf, B. Dehay, P. Ramos-Gonzalez, F. De Giorgi, M. Bourdenx, A. Bessede, J. A. Obeso, C. Matute, F. Ichas, E. Bezard, In vitro α-synuclein neurotoxicity and spreading among neurons and astrocytes using Lewy body extracts from Parkinson disease brains. *Neurobiol. Dis.* **103**, 101–112 (2017).
13. A. Recasens, B. Dehay, J. Bove, I. Carballo-Carbajal, S. Dovero, A. Perez-Villalba, P. O. Fernagut, J. Blesa, A. Parent, C. Perier, I. Farinas, J. A. Obeso, E. Bezard, M. Vila, Lewy body extracts from Parkinson disease brains trigger α-synuclein pathology and neurodegeneration in mice and monkeys. *Ann. Neurol.* **75**, 351–362 (2014).
14. M. Bourdenx, A. Nioche, S. Dovero, M.-L. Arotcarena, S. Camus, G. Porras, M.-L. Thiolat, N. P. Rougier, A. Prigent, P. Aubert, S. Bohic, C. Sandt, F. Laferrière, E. Doudnikoff, N. Kruse, B. Mollenhauer, S. Novello, S. Morari, T. Leste-Lasserre, I. Trigo Damas, M. Goillandeau, C. Perier, C. Estrada, N. Garcia-Carrillo, A. Recasens, N. N. Vaikath, O. M. A. El-Agnaf, M. T. Herrero, P. Derkinderen, M. Vila, J. A. Obeso, B. Dehay, E. Bezard, Identification of distinct pathological signatures induced by patient-derived α-synuclein structures in nonhuman primates. *Sci. Adv.* **6**, eaaz9165 (2020).
15. M. L. Arotcarena, S. Dovero, A. Prigent, M. Bourdenx, S. Camus, G. Porras, M. L. Thiolat, M. Tasselli, P. Aubert, N. Kruse, B. Mollenhauer, I. Trigo Damas, C. Estrada, N. Garcia-Carrillo, N. N. Vaikath, O. M. A. El-Agnaf, M. T. Herrero, M. Vila, J. A. Obeso, P. Derkinderen, B. Dehay, E. Bezard, Bidirectional gut-to-brain and brain-to-gut propagation of synucleinopathy in non-human primates. *Brain* **143**, 1462–1475 (2020).
16. M. Teil, S. Dovero, M. Bourdenx, M. L. Arotcarena, M. Darricau, G. Porras, M. L. Thiolat, I. Trigo-Damas, C. Perier, C. Estrada, N. Garcia-Carrillo, M. T. Herrero, M. Vila, J. A. Obeso, E. Bezard, B. Dehay, Cortical Lewy body injections induce long-distance pathogenic alterations in the non-human primate brain. *NPJ Parkinsons Dis.* **9**, 135 (2023).
17. E. Bezard, S. Dovero, C. Prunier, P. Ravenscroft, S. Chalon, D. Guilloteau, A. R. Crossman, B. Bioulac, J. M. Brotchie, C. E. Gross, Relationship between the appearance of symptoms and the level of nigrostriatal degeneration in a progressive 1-methyl-4-phenyl-1,2,3,6-tetrahydropyridine-lesioned macaque model of Parkinson's disease. *J. Neurosci.* **21**, 6853–6861 (2001).
18. O. Hornykiewicz, Biochemical aspects of Parkinson's disease. *Neurology* **51**, S2–S9 (1998).
19. P. Garcia-Esparcia, K. Hernández-Ortega, B. Ansoleaga, M. Carmona, I. Ferrer, Purine metabolism gene deregulation in Parkinson's disease. *Neuropathol. Appl. Neurobiol.* **41**, 926–940 (2015).
20. S. Zhai, A. Tanimura, S. M. Graves, W. Shen, D. J. Surmeier, Striatal synapses, circuits, and Parkinson's disease. *Curr. Opin. Neurobiol.* **48**, 9–16 (2018).
21. G. M. Runwal, R. H. Edwards, The role of α-synuclein in exocytosis. *Exp. Neurol.* **373**, 114668 (2024).
22. V. Paget-Blanc, M. E. Pfeffer, M. Pronot, P. Lapios, M. F. Angelo, R. Walle, F. P. Cordelières, F. Levet, S. Claverol, S. Lacomme, M. Petrel, C. Martin, V. Pitard, V. De Smedt Peyrusse, T. Biederer, D. Perrais, P. Trifilieff, E. Herzog, A synaptomic analysis reveals dopamine hub synapses in the mouse striatum. *Nat. Commun.* **13**, 3102 (2022).
23. E. Schleiff, J. L. Turnbull, Functional and structural properties of the mitochondrial outer membrane receptor Tom20. *Biochemistry* **37**, 13043–13051 (1998).
24. R. Anand, T. Wai, M. J. Baker, N. Kladt, A. C. Schauss, E. Rugarli, T. Langer, The i-AAA protease YME1L and OMA1 cleave OPA1 to balance mitochondrial fusion and fission. *J. Cell Biol.* **204**, 919–929 (2014).
25. W. Chen, H. Zhao, Y. Li, Mitochondrial dynamics in health and disease: Mechanisms and potential targets. *Signal Transduct. Target. Ther.* **8**, 333 (2023).
26. V. Del Dotto, M. Fogazza, V. Carelli, M. Rugolo, C. Zanna, Eight human OPA1 isoforms, long and short: What are they for? *Biochim. Biophys. Acta Bioenerg.* **1859**, 263–269 (2018).
27. V. Del Dotto, P. Mishra, S. Vidoni, M. Fogazza, A. Maresca, L. Caporali, J. M. McCaffery, M. Cappelletti, E. Baruffini, G. Lenaers, D. Chan, M. Rugolo, V. Carelli, C. Zanna, OPA1

isoforms in the hierarchical organization of mitochondrial functions. *Cell Rep.* **19**, 2557–2571 (2017).

28. S. N. Haber, The primate basal ganglia: Parallel and integrative networks. *J. Chem. Neuroanat.* **26**, 317–330 (2003).

29. J. Pasquini, R. Durcan, L. Wiblin, M. Gersel Stokholm, L. Rochester, D. J. Brooks, D. Burn, N. Pavese, Clinical implications of early caudate dysfunction in Parkinson's disease. *J. Neurol. Neurosurg. Psychiatry* **90**, 1098–1104 (2019).

30. G. V. Sawle, E. D. Playford, D. J. Burn, V. J. Cunningham, D. J. Brooks, Separating Parkinson's disease from normality. Discriminant function analysis of fluorodopa F 18 positron emission tomography data. *Arch. Neurol.* **51**, 237–243 (1994).

31. M. C. Ruppert, A. Greuel, M. Tahmasian, F. Schwartz, S. Stürmer, F. Maier, J. Hammes, M. Tittgemeyer, L. Timmermann, T. van Eimeren, A. Drzezga, C. Eggers, Network degeneration in Parkinson's disease: Multimodal imaging of nigro-striato-cortical dysfunction. *Brain* **143**, 944–959 (2020).

32. N. D'Cruz, G. Vervoort, S. Chalavi, B. W. Dijkstra, M. Gilat, A. Nieuwboer, Thalamic morphology predicts the onset of freezing of gait in Parkinson's disease. *NPJ Parkinsons Dis.* **7**, 20 (2021).

33. E. Dadgar-Kiani, G. Bieri, R. Melki, A. D. Gitler, J. H. Lee, Mesoscale connections and gene expression empower whole-brain modeling of α-synuclein spread, aggregation, and decay dynamics. *Cell Rep.* **41**, 111631 (2022).

34. M. X. Henderson, E. J. Cornblath, A. Darwich, B. Zhang, H. Brown, R. J. Gathagan, R. M. Sandler, D. S. Bassett, J. Q. Trojanowski, V. M. Y. Lee, Spread of α-synuclein pathology through the brain connectome is modulated by selective vulnerability and predicted by network analysis. *Nat. Neurosci.* **22**, 1248–1257 (2019).

35. S. Pandya, Y. Zeighami, B. Freeze, M. Dadar, D. L. Collins, A. Dagher, A. Raj, Predictive model of spread of Parkinson's pathology using network diffusion. *Neuroimage* **192**, 178–194 (2019).

36. S. H. W. Scheres, B. Ryskeldi-Falcon, M. Goedert, Molecular pathology of neurodegenerative diseases by cryo-EM of amyloids. *Nature* **621**, 701–710 (2023).

37. T. W. Todd, N. N. Islam, C. N. Cook, T. R. Caulfield, L. Petrucelli, Cryo-EM structures of pathogenic fibrils and their impact on neurodegenerative disease research. *Neuron* **112**, 2269–2288 (2024).

38. D. Emin, Y. P. Zhang, E. Lobanova, A. Miller, X. Li, Z. Xia, H. Dakin, D. I. Sideris, J. Y. L. Lam, R. T. Ranasinghe, A. Kouli, Y. Zhao, S. De, T. P. J. Knowles, M. Vendruscolo, F. S. Ruggeri, F. I. Aigbirhio, C. H. Williams-Gray, D. Klenerman, Small soluble α-synuclein aggregates are the toxic species in Parkinson's disease. *Nat. Commun.* **13**, 5512 (2022).

39. J. E. Nash, T. H. Johnston, G. L. Collingridge, C. C. Garner, J. M. Brotchie, Subcellular redistribution of the synapse-associated proteins PSD-95 and SAP97 in animal models of Parkinson's disease and L-DOPA-induced dyskinesia. *FASEB J.* **19**, 583–585 (2005).

40. M. L. Kramer, W. J. Schulz-Schaeffer, Presynaptic α-synuclein aggregates, not Lewy bodies, cause neurodegeneration in dementia with Lewy bodies. *J. Neurosci.* **27**, 1405–1410 (2007).

41. D. Scott, S. Roy, α-Synuclein inhibits intersynaptic vesicle mobility and maintains recycling-pool homeostasis. *J. Neurosci.* **32**, 10129–10135 (2012).

42. L. Wang, U. Das, D. A. Scott, Y. Tang, P. J. McLean, S. Roy, α-Synuclein multimers cluster synaptic vesicles and attenuate recycling. *Curr Biol.* **24**, 2319–2326 (2014).

43. J. Lautenschläger, A. D. Stephens, G. Fusco, F. Ströhl, N. Curry, M. Zacharopoulou, C. H. Michel, R. Laine, N. Nespovitaya, M. Fantham, D. Pinotsi, W. Zago, P. Fraser, A. Tandon, P. St George-Hyslop, E. Rees, J. J. Phillips, A. De Simone, C. F. Kaminski, G. S. K. Schierle, C-terminal calcium binding of α-synuclein modulates synaptic vesicle interaction. *Nat. Commun.* **9**, 712 (2018).

44. M. Bartl, J. Nilsson, M. Dakna, S. Weber, S. Schade, M. Xylaki, B. Fernandes Gomes, M. Ernst, M. L. Muntean, F. Sixel-Doring, C. Trenkwalder, H. Zetterberg, A. Brinkmalm, B. Mollenhauer, Lysosomal and synaptic dysfunction markers in longitudinal cerebrospinal fluid of de novo Parkinson's disease. *NPJ Parkinsons Dis.* **10**, 102 (2024).

45. M. T. Henrich, W. H. Oertel, D. J. Surmeier, F. F. Geibl, Mitochondrial dysfunction in Parkinson's disease – A key disease hallmark with therapeutic potential. *Mol. Neurodegener.* **18**, 83 (2023).

46. F. F. Geibl, M. T. Henrich, Z. Xie, E. Zampese, T. Tkatch, D. L. Wokosin, E. Nasiri, C. A. Grotmann, V. L. Dawson, T. M. Dawson, N. S. Chandel, W. H. Oertel, D. J. Surmeier, α-Synuclein pathology disrupts mitochondrial function in dopaminergic and cholinergic neurons at-risk in Parkinson's disease. bioRxiv 571045 [Preprint] (2023). https://doi.org/10.1101/2023.12.11.571045.

47. M. L. Choi, A. Chappard, B. P. Singh, C. Maclachlan, M. Rodrigues, E. I. Fedotova, A. V. Berezhnov, S. De, C. J. Peddie, D. Athauda, G. S. Virdi, W. Zhang, J. R. Evans, A. I. Wernick, Z. S. Zanjani, P. R. Angelova, N. Esteras, A. Y. Vinokurov, K. Morris, K. Jeacock, L. Tosatto, D. Little, P. Gissen, D. J. Clarke, T. Kunath, L. Collinson, D. Klenerman, A. Y. Abramov, M. H. Horrocks, S. Gandhi, Pathological structural conversion of α-synuclein at the mitochondria induces neuronal toxicity. *Nat. Neurosci.* **25**, 1134–1148 (2022).

48. B. R. De Miranda, E. M. Rocha, S. L. Castro, J. T. Greenamyre, Protection from α-Synuclein induced dopaminergic neurodegeneration by overexpression of the mitochondrial import receptor TOM20. *NPJ Parkinsons Dis* **6**, 38 (2020).

49. F. Burté, V. Carelli, P. F. Chinnery, P. Yu-Wai-Man, Disturbed mitochondrial dynamics and neurodegenerative disorders. *Nat. Rev. Neurol.* **11**, 11–24 (2015).

50. N. Ishihara, Y. Fujita, T. Oka, K. Mihara, Regulation of mitochondrial morphology through proteolytic cleavage of OPA1. *EMBO J.* **25**, 2966–2977 (2006).

51. J. H. Martínez, F. Fuentes, V. Vanasco, S. Alvarez, A. Alaimo, A. Cassina, F. Coluccio Leskow, F. Velazquez, Alpha-synuclein mitochondrial interaction leads to irreversible translocation and complex I impairment. *Arch. Biochem. Biophys.* **651**, 1–12 (2018).

52. M. Robotta, H. R. Gerding, A. Vogel, K. Hauser, S. Schildknecht, C. Karreman, M. Leist, V. Subramaniam, M. Drescher, Alpha-synuclein binds to the inner membrane of mitochondria in an α-helical conformation. *Chembiochem* **15**, 2499–2502 (2014).

53. R. Di Maio, P. J. Barrett, E. K. Hoffman, C. W. Barrett, A. Zharikov, A. Borah, X. Hu, J. McCoy, C. T. Chu, E. A. Burton, T. G. Hastings, J. T. Greenamyre, α-Synuclein binds to TOM20 and inhibits mitochondrial protein import in Parkinson's disease. *Sci. Transl. Med.* **8**, 342ra378 (2016).

54. T. M. Goralski, L. Meyerdirk, L. Breton, L. Brasseur, K. Kurgat, D. DeWeerd, L. Turner, K. Becker, M. Adams, D. J. Newhouse, M. X. Henderson, Spatial transcriptomics reveals molecular dysfunction associated with cortical Lewy pathology. *Nat. Commun.* **15**, 2642 (2024).

55. N. W. Kowall, P. Hantraye, E. Brouillet, M. F. Beal, A. C. McKee, R. J. Ferrante, MPTP induces alpha-synuclein aggregation in the substantia nigra of baboons. *Neuroreport* **11**, 211–213 (2000).

56. D. A. McRitchie, H. Cartwright, S. M. Pond, C. J. van der Schyf, N. Castagnoli Jr., D. G. van der Nest, G. M. Halliday, The midbrain dopaminergic cell groups in the baboon Papio ursinus. *Brain Res. Bull.* **47**, 611–623 (1998).

57. F. N. Soria, C. Paviolo, E. Doudnikoff, M. L. Arotcarena, A. Lee, N. Danne, A. K. Mandal, P. Gosset, B. Dehay, L. Groc, L. Cognet, E. Bezard, Synucleinopathy alters nanoscale organization and diffusion in the brain extracellular space through hyaluronan remodeling. *Nat. Commun.* **11**, 3440 (2020).

58. M. R. Ahmed, A. Berthet, E. Bychkov, G. Porras, Q. Li, B. H. Bioulac, Y. T. Carl, B. Bloch, S. Kook, I. Aubert, S. Dovero, E. Doudnikoff, V. V. Gurevich, E. V. Gurevich, E. Bezard, Lentiviral overexpression of GRK6 alleviates L-dopa-induced dyskinesia in experimental Parkinson's disease. *Sci. Transl. Med.* **2**, 28ra28 (2010).

59. S. George, S. S. Mok, S. Nurjono, S. Ayton, D. I. Finkelstein, C. L. Masters, Q. X. Li, J. G. Culvenor, α-Synuclein transgenic mice reveal compensatory increases in Parkinson's disease-associated proteins DJ-1 and parkin and have enhanced α-synuclein and PINK1 levels after rotenone treatment. *J. Mol. Neurosci.* **42**, 243–254 (2010).

60. K. E. Paleologou, A. Oueslati, G. Shakked, C. C. Rospigliosi, H. Y. Kim, G. R. Lamberto, C. O. Fernandez, A. Schmid, F. Chegini, W. P. Gai, D. Chiappe, M. Moniatte, B. L. Schneider, P. Aebischer, D. Eliezer, M. Zweckstetter, E. Masliah, H. A. Lashuel, Phosphorylation at S87 is enhanced in synucleinopathies, inhibits α-synuclein oligomerization, and influences synuclein-membrane interactions. *J. Neurosci.* **30**, 3184–3198 (2010).

61. W. Peelaerts, L. Bousset, A. Van der Perren, A. Moskalyuk, R. Pulizzi, M. Giugliano, C. Van den Haute, R. Melki, V. Baekelandt, α-Synuclein strains cause distinct synucleinopathies after local and systemic administration. *Nature* **522**, 340–344 (2015).

62. N. Landeck, H. Hall, M. T. Ardah, N. K. Majbour, O. M. El-Agnaf, G. Halliday, D. Kirik, A novel multiplex assay for simultaneous quantification of total and S129 phosphorylated human alpha-synuclein. *Mol. Neurodegener.* **11**, 61 (2016).

63. S. H. Shahmoradian, A. J. Lewis, C. Genoud, J. Hench, T. E. Moors, P. P. Navarro, D. Castano-Diez, G. Schweighauser, A. Graff-Meyer, K. N. Goldie, R. Sutterlin, E. Huisman, A. Ingrassia, Y. Gier, A. J. M. Rozemuller, J. Wang, A. Paepe, J. Erny, A. Staempfli, J. Hoernschemeyer, F. Grosseruschkamp, D. Niedieker, S. F. El-Mashtoly, M. Quadri, I. W. F. J. Van, V. Bonifati, K. Gerwert, B. Bohrmann, S. Frank, M. Britschgi, H. Stahlberg, W. D. J. Van de Berg, M. E. Lauer, Lewy pathology in Parkinson's disease consists of crowded organelles and lipid membranes. *Nat. Neurosci.* **22**, 1099–1109 (2019).

64. A. Van der Perren, G. Gelders, A. Fenyi, L. Bousset, F. Brito, W. Peelaerts, C. Van den Haute, S. Gentleman, R. Melki, V. Baekelandt, The structural differences between patient-derived α-synuclein strains dictate characteristics of Parkinson's disease, multiple system atrophy and dementia with Lewy bodies. *Acta Neuropathol.* **139**, 977–1000 (2020).

65. N. M. Jensen, Y. Fu, C. Betzer, H. Li, S. Elfarrash, A. H. Shaib, D. Krah, Z. Vitic, L. Reimer, H. Gram, V. Buchman, M. Denham, S. O. Rizzoli, G. M. Halliday, P. H. Jensen, MJF-14 proximity ligation assay detects early non-inclusion alpha-synuclein pathology with enhanced specificity and sensitivity. *NPJ Parkinsons Dis.* **10**, 227 (2024).

66. I. Liekniņa, L. Reimer, T. Panteļejevs, A. Lends, K. Jaudzems, A. El-Turabi, H. Gram, A. Hammi, P. H. Jensen, K. Tārs, Structural basis of epitope recognition by anti-alpha-synuclein antibodies MJFR14-6-4-2. *NPJ Parkinsons Dis.* **10**, 206 (2024).

67. M. Bourdenx, S. Dovero, M. Engeln, S. Bido, M. F. Bastide, N. Dutheil, I. Vollenweider, L. Baud, C. Piron, V. Grouthier, T. Boraud, G. Porras, Q. Li, V. Baekelandt, D. Scheller, A. Michel, P. O. Fernagut, F. Georges, G. Courtine, E. Bezard, B. Dehay, Lack of additive role of ageing in nigrostriatal neurodegeneration triggered by α-synuclein overexpression. *Acta Neuropathol. Commun.* **3**, 46 (2015).

68. J. P. Anderson, D. E. Walker, J. M. Goldstein, R. de Laat, K. Banducci, R. J. Caccavello, R. Barbour, J. Huang, K. Kling, M. Lee, L. Diep, P. S. Keim, X. Shen, T. Chataway,

M. G. Schlossmacher, P. Seubert, D. Schenk, S. Sinha, W. P. Gai, T. J. Chilcote, Phosphorylation of Ser-129 is the dominant pathological modification of α-synuclein in familial and sporadic Lewy body disease. *J. Biol. Chem.* **281**, 29739–29752 (2006).

69. J. Altmann, Observational study of behavior: Sampling methods. *Behaviour* **49**, 227–266 (1974).

70. S. M. Camus, C. Blois-Heulin, Q. Li, M. Hausberger, E. Bezard, Behavioural profiles in captive-bred cynomolgus macaques: Towards monkey models of mental disorders? *PLOS One* **8**, e62141 (2013).

71. S. M. Camus, C. Rochais, C. Blois-Heulin, Q. Li, M. Hausberger, E. Bezard, Birth origin differentially affects depressive-like behaviours: Are captive-born cynomolgus monkeys more vulnerable to depression than their wild-born counterparts? *PLOS ONE* **8**, e67711 (2013).

72. S. M. J. Camus, C. Rochais, C. Blois-Heulin, Q. Li, M. Hausberger, E. Bezard, Depressive-like behavioral profiles in captive-bred single- and socially-housed rhesus and cynomolgus macaques: A species comparison. *Front. Behav. Neurosci.* **8**, 47 (2014).

73. M. Bourdenx, N. S. Koulakiotis, D. Sanoudou, E. Bezard, B. Dehay, A. Tsarbopoulos, Protein aggregation and neurodegeneration in prototypical neurodegenerative diseases: Examples of amyloidopathies, tauopathies and synucleinopathies. *Prog. Neurobiol.* **155**, 171–193 (2017).

74. N. N. Vaikath, N. K. Majbour, K. E. Paleologou, M. T. Ardah, E. van Dam, W. D. van de Berg, S. L. Forrest, L. Parkkinen, W. P. Gai, N. Hattori, M. Takanashi, S. J. Lee, D. M. Mann, Y. Imai, G. M. Halliday, J. Y. Li, O. M. El-Agnaf, Generation and characterization of novel conformation-specific monoclonal antibodies for α-synuclein pathology. *Neurobiol. Dis.* **79**, 81–99 (2015).

75. B. I. Giasson, R. Jakes, M. Goedert, J. E. Duda, S. Leight, J. Q. Trojanowski, V. M. Lee, A panel of epitope-specific antibodies detects protein domains distributed throughout human α-synuclein in Lewy bodies of Parkinson's disease. *J. Neurosci. Res.* **59**, 528–533 (2000).

76. J. Ho, T. Tumkaya, S. Aryal, H. Choi, A. Claridge-Chang, Moving beyond P values: Data analysis with estimation graphics. *Nat. Methods* **16**, 565–566 (2019).